AD_____

Award Number: W81XWH-09-1-0062

TITLE: Image Based Biomarker of Breast Cancer Risk: Analysis of Risk Disparity among Minority Populations

PRINCIPAL INVESTIGATOR: Fengshan Liu, Ph.D., Xiquan Shi, Ph.D., Charlie Wilson, Ph.D., Dragoljub Pokrajac, Ph.D., Predrag Bakic, Ph.D., Andrew Maidment, Ph.D.

CONTRACTING ORGANIZATION:
Delaware State University

Dover, DE 19901

REPORT DATE: March 2013

TYPE OF REPORT: Annual

PREPARED FOR: U.S. Army Medical Research and Materiel Command
               Fort Detrick, Maryland 21702-5012

DISTRIBUTION STATEMENT: (Check one)

■ Approved for public release; distribution unlimited

The views, opinions and/or findings contained in this report are those of the author(s) and should not be construed as an official Department of the Army position, policy or decision unless so designated by other documentation.

REPORT DOCUMENTATION PAGE

Form Approved
OMB No. 0704-0188

1. REPORT DATE	2. REPORT TYPE	3. DATES COVERED
March 2013	Annual	1 March 2012 – 28 February 2013

4. TITLE AND SUBTITLE	5a. CONTRACT NUMBER
Image Based Biomarker of Breast Cancer Risk: Analysis of Risk Disparity among Minority Populations	5b. GRANT NUMBER W81XWH-09-1-0062
	5c. PROGRAM ELEMENT NUMBER

6. AUTHOR(S)	5d. PROJECT NUMBER
Fengshan Liu, Xiquan Shi, Charlie, Wilson, Dragoljub Pokrajac, Predrag Bakic, Andrew Maidment	5e. TASK NUMBER
E-Mail: fliu@desu.edu	5f. WORK UNIT NUMBER

7. PERFORMING ORGANIZATION NAME(S) AND ADDRESS(ES)	8. PERFORMING ORGANIZATION REPORT NUMBER
Delaware State University Dover, DE 19901	

9. SPONSORING / MONITORING AGENCY NAME(S) AND ADDRESS(ES)	10. SPONSOR/MONITOR'S ACRONYM(S)
U.S. Army Medical Research and Materiel Command Fort Detrick, Maryland 21702-5012	
	11. SPONSOR/MONITOR'S REPORT NUMBER(S)

12. DISTRIBUTION / AVAILABILITY STATEMENT
Approved for Public Release; Distribution Unlimited

13. SUPPLEMENTARY NOTES

14. ABSTRACT

This year we continue our partnership between Delaware State University and University of Pennsylvania. We finalized ACRIN data transfer on MIRC and resolved issues with various batch transfers. We performed a preliminary query of the ACRIN data aimed at identifying the prevalence of women with incomplete visualization of the breast. We developed a code to estimate the breast cancer risks using the demographic metadata information from the ACRIN cases. We estimated breast densities for GE mammograms from the ACRIN database, using the software developed at the University of Pennsylvania. A novel breast image registration method is proposed to obtain a composite mammogram from several images with partial breast coverage, for the purpose of accurate breast density estimation. We designed a method to improve thickness control of the Cooper's ligaments in the simulation algorithm by reducing "dents" on the ligaments' surface.

15. SUBJECT TERMS
Breast Cancer, Risk Disparity, Minority Population, Image-Based Biomarker, Training Program

16. SECURITY CLASSIFICATION OF:			17. LIMITATION OF ABSTRACT	18. NUMBER OF PAGES	19a. NAME OF RESPONSIBLE PERSON USAMRMC
a. REPORT	b. ABSTRACT	c. THIS PAGE			19b. TELEPHONE NUMBER *(include area code)*
U	U	U	UU	47	

Table of Contents

1. Introduction

This year we continue our partnership between Delaware State University and University of Pennsylvania. We finalized ACRIN data transfer on MIRC and resolved issues with various batch transfers. We performed a preliminary query of the ACRIN data aimed at identifying the prevalence of women with incomplete visualization of the breast. We developed a code to estimate the breast cancer risks using the demographic metadata information from the ACRIN cases. We estimated breast densities for GE mammograms from the ACRIN database, using the software developed at the University of Pennsylvania. A novel breast image registration method is proposed to obtain a composite mammogram from several images with partial breast coverage, for the purpose of accurate breast density estimation. We designed a method to improve thickness control of the Cooper's ligaments in the simulation algorithm by reducing "dents" on the ligaments' surface.

2. Body

With this funded project, we will enhance DSU breast cancer research resources by: improving our expertise in translational and clinical breast cancer research; developing methods for computing image-based biomarkers for breast cancer risk, as well as methods for biomarker analysis of risk disparity; developing a database of clinical biomarkers computed from images of minority women; refining the existing and developing novel data mining techniques to determine the relationship between risk and image-based biomarkers. The improvement will support further growth of a sustained breast cancer research program at DSU and help establish us as a mid-Atlantic center for analysis of breast cancer risk and risk disparity among minority women.

The specific objectives of this training program include: (1) extending the skills of a select cadre of DSU faculty, so that they may become accomplished, influential and competitive breast cancer researchers; (2) establishing an independent breast cancer research program at DSU by performing a joint DSU–UPENN research project focused on breast cancer risk disparity in minority populations; and (3) producing a corpus of high quality published work and develop a portfolio of independently funded research grants at DSU to support a sustained breast cancer research program.

2.1 Objective 1

Extend the skills of a select cadre of Delaware State University (DSU) faculty, so that we may become accomplished, influential, and competitive breast cancer researchers.

- Organize specific training for selected DSU faculty, aimed at complementing our individual scientific background. (Y1-4); and

- Augment the faculty training by frequent communications with collaborating mentors and other renowned breast cancer researchers, by: (Y1-4)

2.1.1 Seminars and Conferences attended

- On July 8-11, 2012, Dr. Pokrajac and Mr. Chen attended and presented the IWDM 2012, the 11th International Workshop on Breast Imaging, in Philadelphia, PA.

  The first presentation entitled "Toward Breast Anatomy Simulation using GPU" (co-authored by J. Chu, D. Pokrajac, A. D. Maidment, P. Bakic) described the development of highly-parallel GPU simulation of software breast phantoms.

  The second presentation entitled "Simulation of Three Materials Partial Volume Averaging in a Software Breast Phantom" (co-authored by F. Chen, **D. Pokrajac**, X. Shi, F. Liu, A. D. Maidment, P. Bakic) described the development of simulation for voxels containing three different materials in a software phantom.

These two presentations are also published in Springer *Lecture Notes in Computer Science* 7361, edited by Gavenonis, Sara, Bakic, Predrag R. and Maidment, Andrew D.A., 2012.

- On February 9-14, 2013, Dr. Pokrajac attended and presented the 2013 SPIE Medical Imaging conference in Orlando, FL.

  The first presentation entitled "Breast image registration by using non-linear local affine transformation" (co-authored by F. Chen, P. Zheng, P. Xu, D. Pokrajac, P. R. Bakic, Andrew D. A. Maidment, F. Liu, X. Shi) discusses a novel method for registration of mammograms.

  The second presentation entitled "Two methods for simulation of dense tissue distribution in software breast phantoms," (co-authored by J. Chui, R. Zeng, D. Pokrajac, S. Park, K. J. Myers, A. D. A. Maidment, P. R. Bakic) described the comparison of two techniques for simulation of dense tissue distribution with the distribution from clinical images.

These two presentations are also published in **Proceedings of SPIE Volume 8668**, *2013*.

2.1.2 DSUPENN Breast Cancer Seminar

Task-based strategy for optimized contrast enhanced breast imaging: Analysis of six imaging techniques for mammography and tomosynthesis, January 17, 2013
Speaker:
Lynda Ikejimba,
Medical Physics Graduate Program
Ravin Advanced Imaging Laboratories
Duke University

2.2 Objective 2

Establish an independent breast cancer research program at DSU by performing a joint DSU/Penn research project focused on breast cancer risk disparity in minority populations

- Obtain appropriate IRB approvals for the proposed research. (months 1-6 of Y1)

- Included in Year 1 Report.

- Develop a database of anonymized clinical mammograms and patient metadata, obtained retrospectively from ACRIN DMIST and Penn PPG trials. (Y1-Y2)

- Included in Year 2 Report.

- Exploratory study (Drs. Wilson, Pokrajac, and Liu) Explore potential racial differences in genetic determinants of breast density. (Y2-Y4)

2.2.1   Analysis of Mammographic Images and Clinical Metadata of All Minority Women and the Age-Matched Caucasian Controls from the ACRIN DMIST Database

We finalized ACRIN data transfer on MIRC and resolved issues with various batch transfers. During the transfer some of the studies from ACRIN data were reported as having 'invalid' images, related to problems with encoding in the MIRC database. Some cases did not get merged in the correct MIRC folders. Those cases were reviewed and if needed pushed manually to ensure correct uploading. In addition, the DICOM import service periodically got interrupted, which required to restart the MIRC automatic importing service. VB script problem: XML files from ACRIN Data occasionally did not get parsed correctly.

We performed a preliminary query of the ACRIN data aimed at identifying the prevalence of women with incomplete visualization of the breast. Here is the summary of the results from this query:

- The total number of uploaded cases with more than 4 Dicoms images is 3845; 267 of them are aggregated duplicates (files belong to the same patient but were divided in various folders);

- The number of cases with multiple images (>4) and no aggregation is 3578;

- About 30% of the cases have been checked manually to confirm partial visualization;

- If the number of DICOMs is less than 9, partial visualization is present in about 10% of the cases;

- Our estimation is that that about 500-550 out of 3845 cases have partial breast visualization which is approximately 5-8% of all cases.

- There are 4406 patients who have four or less DICOM images with MLO-position. The algorithm we employed to compute density is more suitable for MLO-position images than CC-position.

We have also developed a code to estimate the breast cancer risks using the demographic metadata information from the ACRIN cases. The risk estimation is based upon the Gail risk model, currently used by the National Cancer Institute. Our code has been developed as a wrapper script around the Java software for the Gail risk estimation (downloaded from the hughesriskapps.net). The risk estimation method uses as its input the patient's age, the age of the menarche, the age of the first live-birth, the number of biopsies, the number of first-degree relatives with cancer; the information about previous biopsies with hyperplasia, and the race. See Figure 7 and Figure 8.

These corresponding information was read from the metadata accompanying the ACRIN database of images. In cases of missing information, we followed the instructions in the Gail risk model and used the "UNKNOWN" entry.

We estimated breast densities for GE mammograms from the ACRIN database, using the software developed at the University of Pennsylvania. The total number of processed images (both MLO and CC) was 24945. For the same images, we calculated risk estimation using the Gail model.

For patients with 2 MLO paired images (left and right) we performed and computed:

- Comparison of Histograms of average and minimal densities for different racial group

- Correlations between estimated minimal and average densities and the lifetime risk estimated by GAIL model for all the samples, and for racial groups

- Scatter plots of estimated densities on left and right breast for all the samples, and for racial groups

- Correlations of estimated densities on L and R images with demographic variables all the samples

- Correlations of estimated densities on L and R images with demographic variables for different racial groups when density was <80%

For patients with more than 2MLO images:

- Correlations between estimated minimal and average densities and the lifetime risk estimated by GAIL model

The preliminary results indicated that there is no sufficient statistical evidence that the distribution of breast densities in African-Americans population differs from the distribution in Caucasian population, see Figure 1 to Figure 4. And the breast density distribution does not vary with age groups, see Figure 5 and Figure 6. The obtained correlations between estimated minimal and average densities and the lifetime risk estimated by GAIL model were small but statistically significant both for general population and for African-Americans, see Figure 7 and Figure 8. Correlations between estimated densities on left and right breasts were high and statistically significant.

If we treat women's breast density as a random variable, after we normalize the frequency and perform interpolation on the histogram graph (see Figure 1), we obtain this probability distribution of breast density (see Figure 2). From the figures, we can see that it is most common that women's breast density is around 25%, and it is unlikely a woman's breast density is around 0%, 80% or 100%. The significance of this plot is to help medical doctors to establish a profile about breast density in order to tell whether a given density case is "normal", "abnormal", "common" or "rare". All of the above show that the probability distribution of breast density, unlike breast volume, remains relatively independent of race and age (see Figure 6).
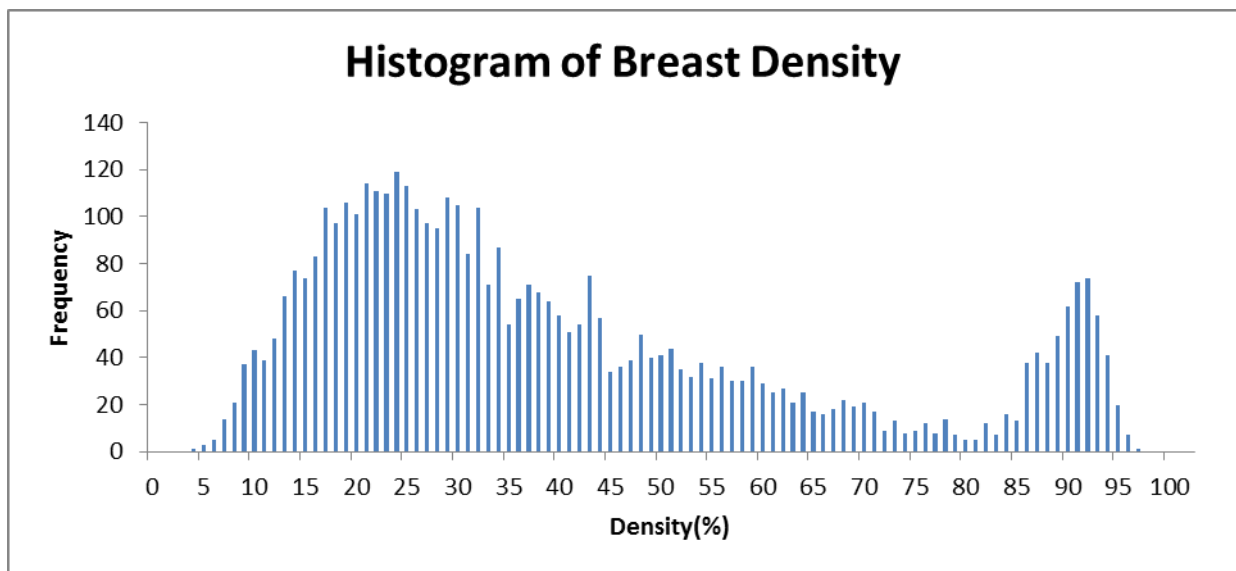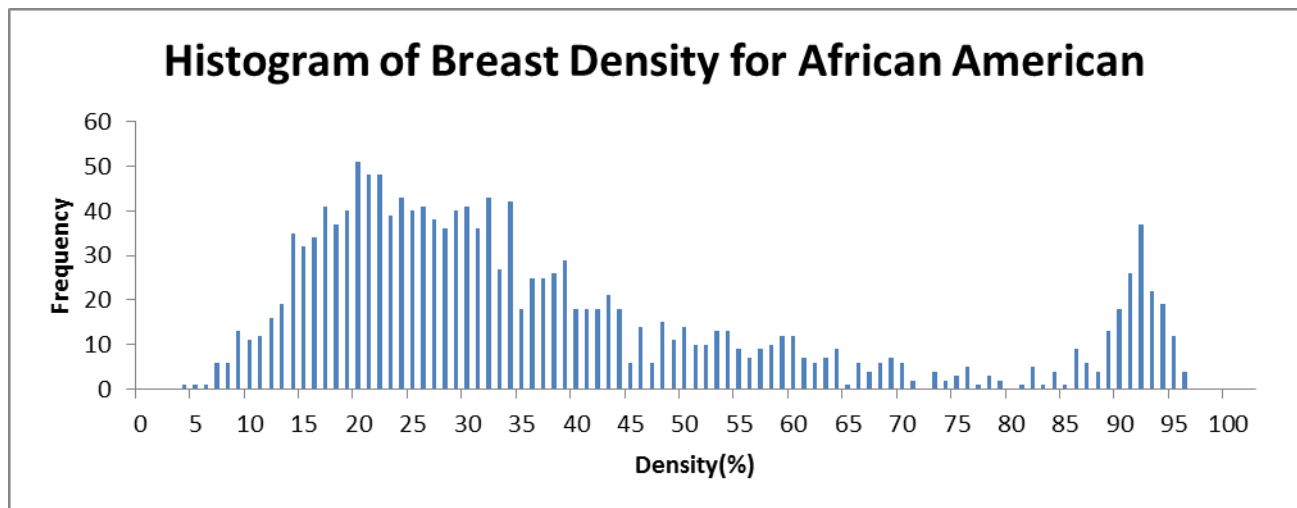

Figure 1 The histogram of breast density computed from all 4406 MLO-position images.
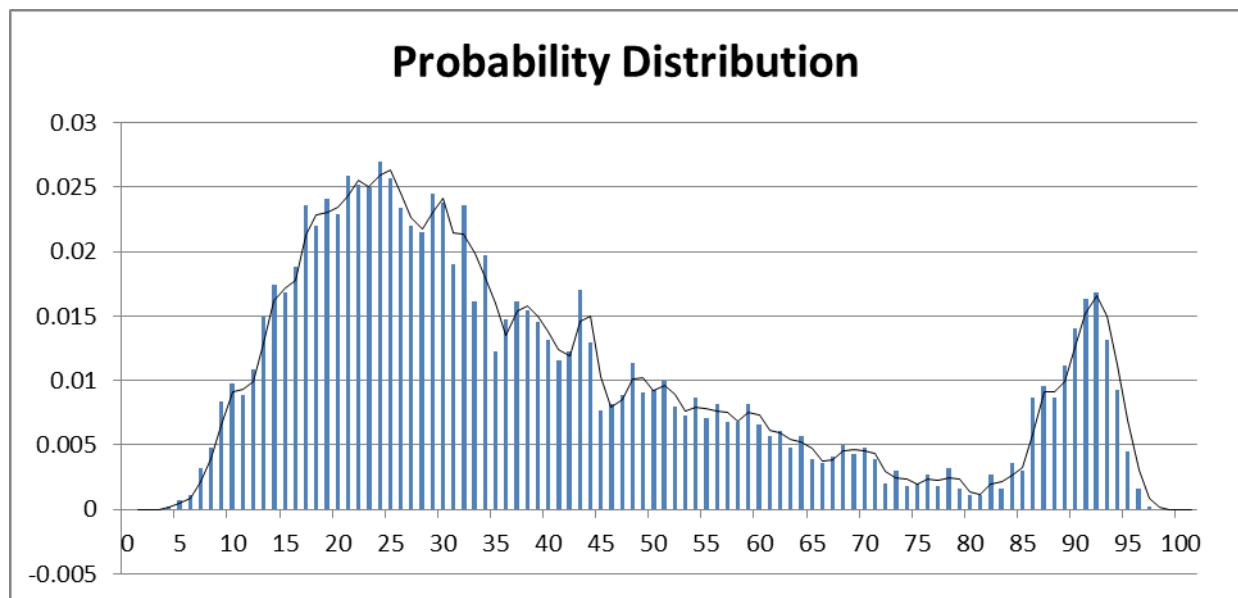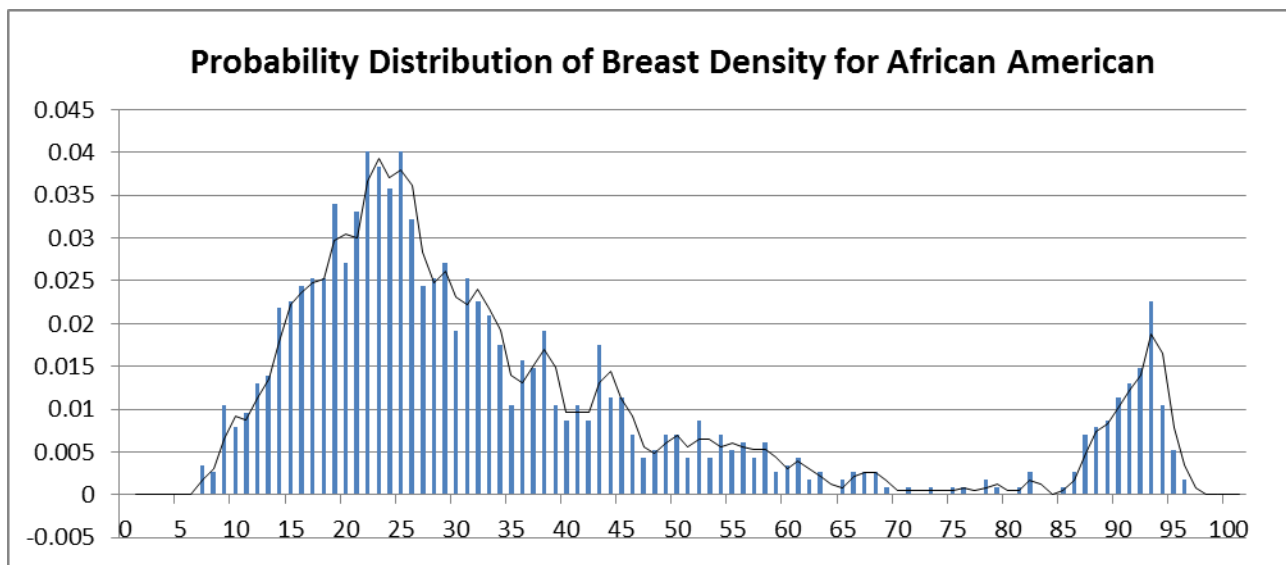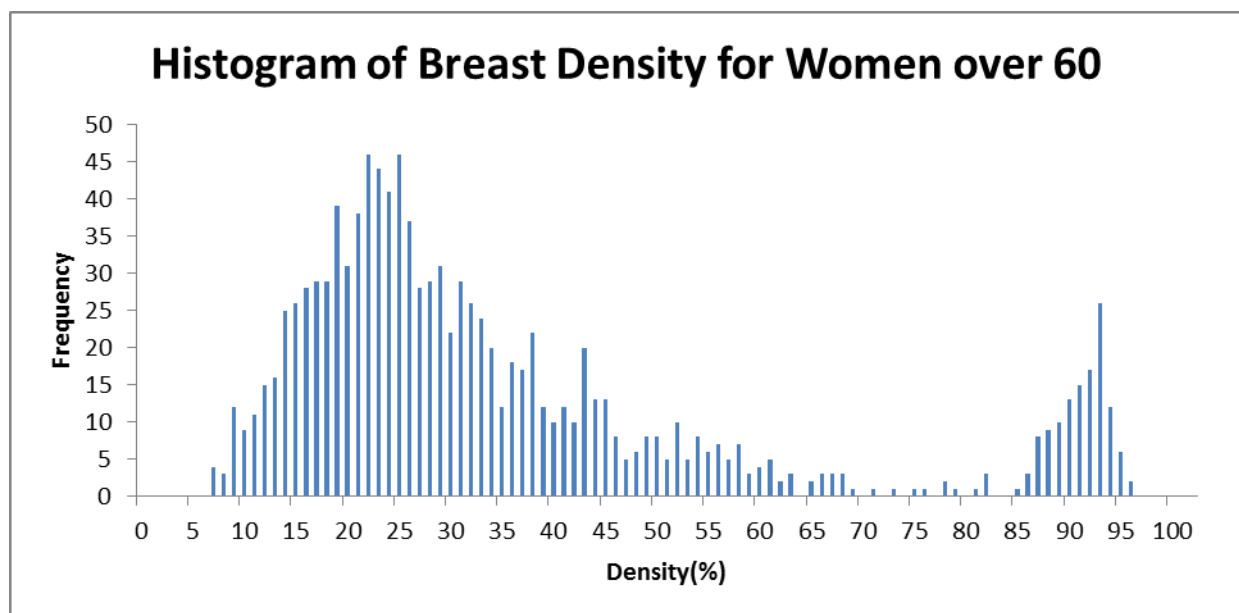
Figure 2 The probability distribution of breast density.

Figure 3 The histogram of breast density for African American. Sample size=1568. It looks similar to Fig 1 for all races combined.

Figure 4 The probability distribution of breast density for African American.

Figure 5 The histogram of breast density of women over 60 years old. Sample size=1147.
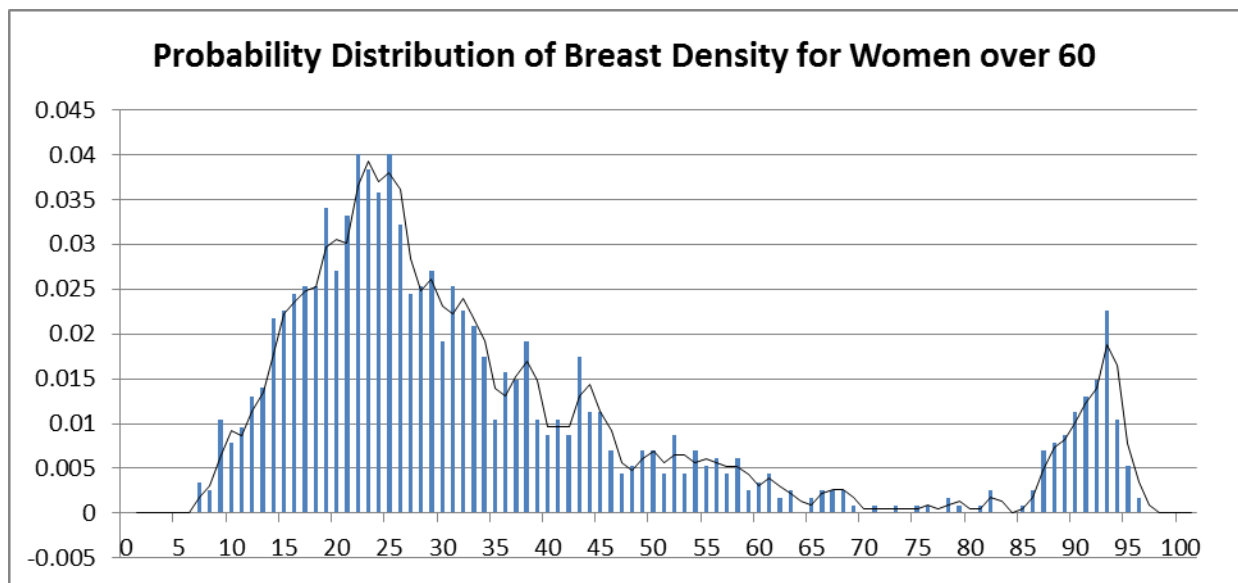
Figure 6 The probability distribution of breast density for women over 60 years old.
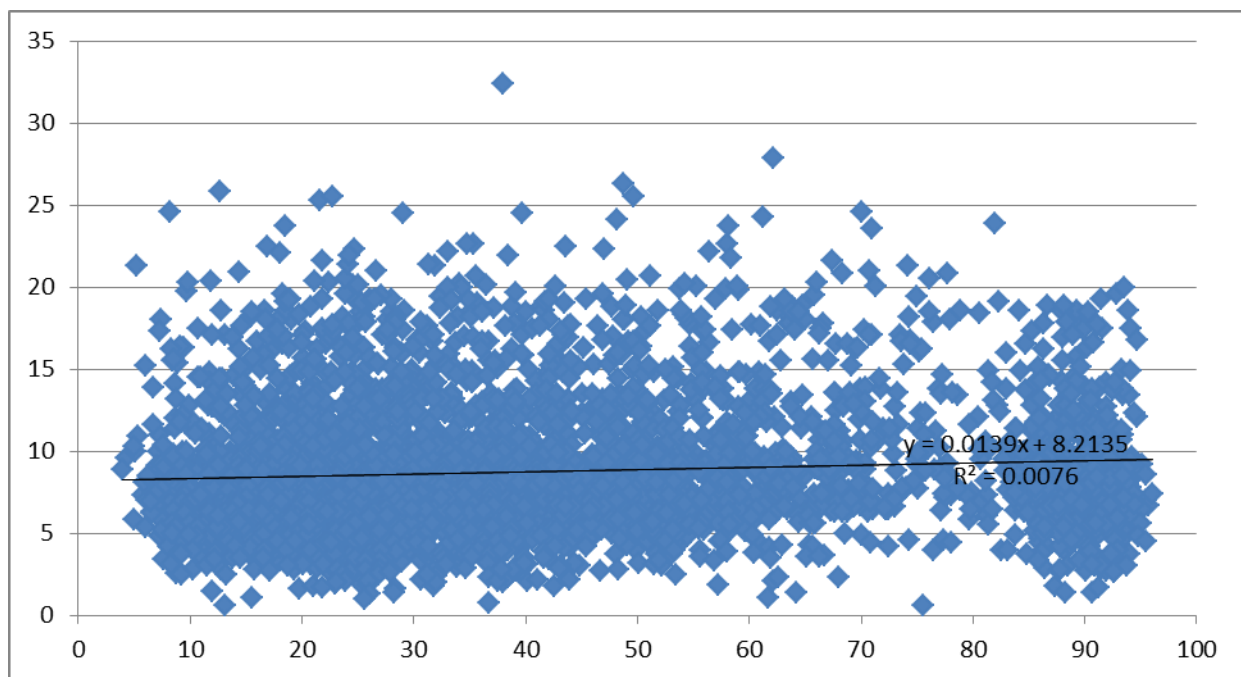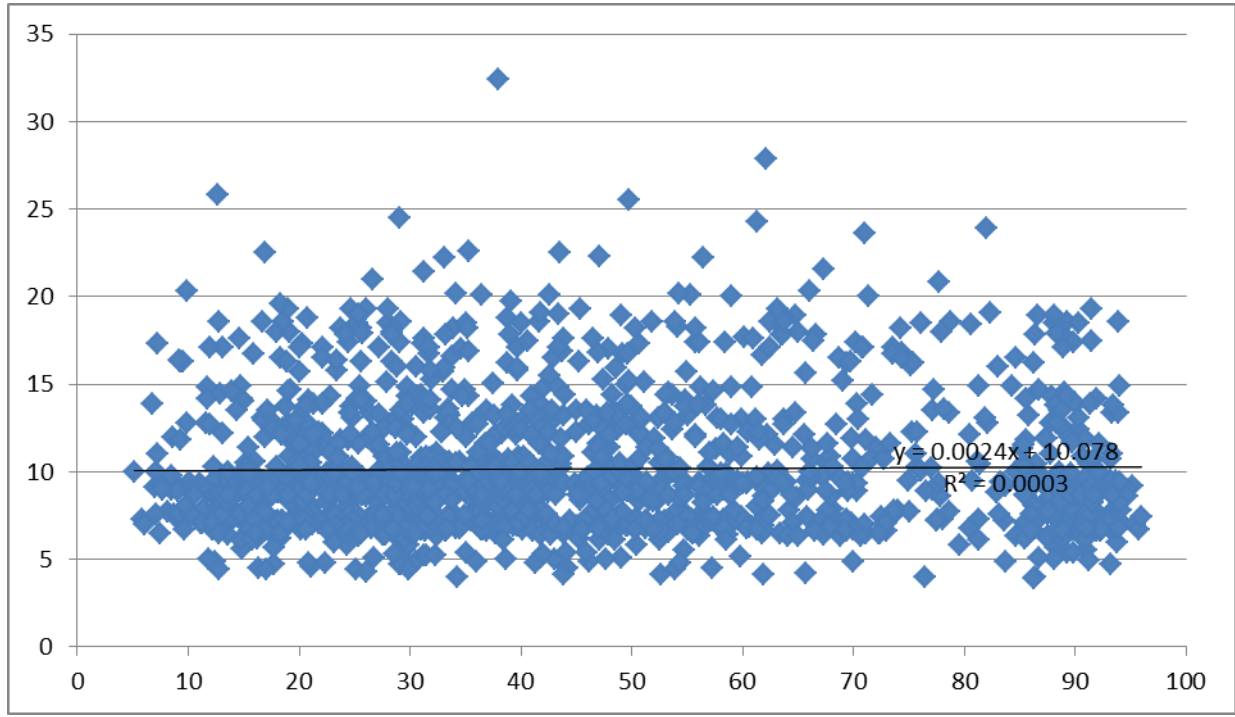

Figure 7 This figure shows that, for all 4406 MLO-position samples, the breast density and the life-time breast cancer risk estimated by using the Gail's model are weakly but significantly correlated to each other .

Figure 8 The correlation is slightly weaker for African Americans.

In Figure 1, the second peak in the range (85%, 96%) seems unnatural, and about 10% of patients have this "suspiciously unnatural" density. This percentage is roughly the percentage of women in the same age window in USA who have plastic surgery of breast. It is also known that the implants affect mammogram in some degree. Therefore, the plastic surgery could be the reason for this "suspicious" peak in the probability distribution. However, we see this peak for all races and all age groups(some are shown below). Therefore, it remains uncertain if the second peak is unnatural.
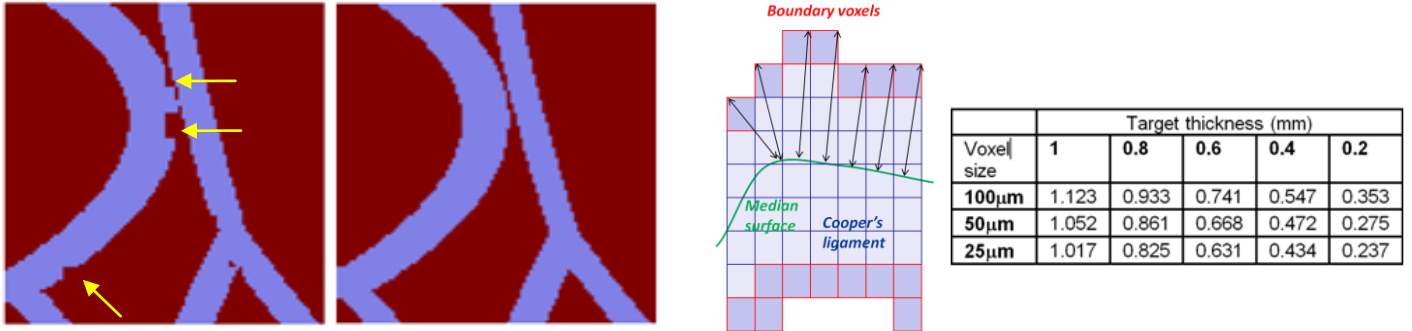
2.2.2 Mammogram Image Registration/Fusion

A novel breast image registration method is proposed to obtain a composite mammogram from several images with partial breast coverage, for the purpose of accurate breast density estimation. The breast percent density estimated as a fractional area occupied by fibroglandular tissue has been shown to be correlated with breast cancer risk. Some mammograms, however, do not cover the whole breast area, which makes the interpretation of breast density estimates ambiguous. One solution is to register and merge mammograms, yielding complete breast coverage. Due to elastic properties of breast tissue and differences in breast positioning and deformation during the acquisition of individual mammograms, the use of linear transformations does not seem appropriate for mammogram registration. Non-linear transformations are limited by the changes in the mammographic projections pixel intensity with different positions of the focal spot. We propose a novel method based upon non-linear local affine transformations. Our algorithm requires that feature points be extracted prior to registration, and the result of registration will depend on the reliability and accuracy of the extracted features. Automatic identification and extraction of feature points is difficult due to the non-linear compression

deformation and the lack of significant landmarks in mammograms . We observe the prominent features (such as ducts and blood vessels) from both images. The crossing points are determined upon visual similarity in both mammograms. Due to compression and different positions of the breast, the coordinates of those crossing points may be different in the two mammograms, but the orientation of feature and local curvature of crossing points are more likely to be preserved. We also select other features (end points and middle points) in a small neighborhood around the selected crossing points. Subsequently, the deformation between two sets of feature points can be estimated. Given two sets of feature points in two images that need to be registered, we assume the deformation between them can be approximated by affine transformation, which can be considered as a first-order approximation of the true transformation resulting from breast projection. Finally, Shepherd interpolation is employed to compute affine transformations for the rest of the image area. The pixel values in the composite image are assigned using bilinear interpolation. We present preliminary results using the proposed approach applied to clinic mammograms taken from the ACRIN DMIST database of mammograms. This work is a part of a larger study of racial disparity in breast cancer risk. For that project, breast percent density and parenchymal texture of minority women and age-matched Caucasian controls from the ACRIN DMIST database are being compared. To date, we have been able to achieve anecdotal results that support continued development and testing of this new method. The proposed method is robust, since the results of registration are similar regardless of the choice of the reference image. The observable features, especially the nipple and the boundary of skin, have good agreement. The results of the proposed method are comparable to the results of the diffeomorphic transform implemented using ANTs, an open source software package. Particularly, the textures of warped image are preserved in registered images, and the shape of registered image is similar as reference image. The registration error is smaller in the region of overlap (the upper part of the registered image), since we can extract the corresponding feature points only from this region. . The proposed transformation can be controlled locally. Moreover, the method is converging to the ground truth deformation if the paired feature points are evenly distributed and its number is large enough .In our future work, we plan to perform more extensive quantitative validation of the proposed algorithm on a series reference and warped images extracted from all the applicable images in the ACRIN DMIST database. Also, we will apply the technique to more images in the ACRIN DMIST database and develop statistical measures of the registration accuracy.

2.2.3 Breast Phantom Development and Characterization

Numerous research contributions have been made related to further development and characterization of the software breast phantom, including the improved simulation of breast Cooper's ligaments, insertion of simulated microcalcification clusters in the phantom, simulation of the dense tissue distribution, and simulation of phantom voxels containing multiple tissues (partial volume simulation). The following details these contributions. We designed a method to improve thickness control of the Cooper's ligaments in the simulation

algorithm by reducing "dents" on the ligaments' surface. The method is based on more accurate determination of the ligament closest to the cubic region and utilization of the exact distance to the ligament instead of the linear approximation. The method is currently under test, see Figure 9.

|	Target thickness (mm)				
Voxel size	1	0.8	0.6	0.4	0.2
100μm	1.123	0.933	0.741	0.547	0.353
50μm	1.052	0.861	0.668	0.472	0.275
25μm	1.017	0.825	0.631	0.434	0.237

Figure 9 (a) Dent-shaped artifacts visible on a section of 100μm phantom; (b) The novel algorithm eliminates the dent-shaped artifact; (c) Measurement of Cooper's ligament thickness; and (d) Target and measured average thicknesses of the ligaments for various phantom resolutions and voxel sizes.

We developed and preliminary tested a method for automatic insertion of simulated calcifications into a voxelized phantom, see Figure 10. Also, we developed an algorithm for insertion of calcifications into an oct-tree based phantom, see Figure 11. We worked on replacement of commercial software for phantom deformation (Abaqus) with open-source and in-house solutions.


(a)   (b)   (c)
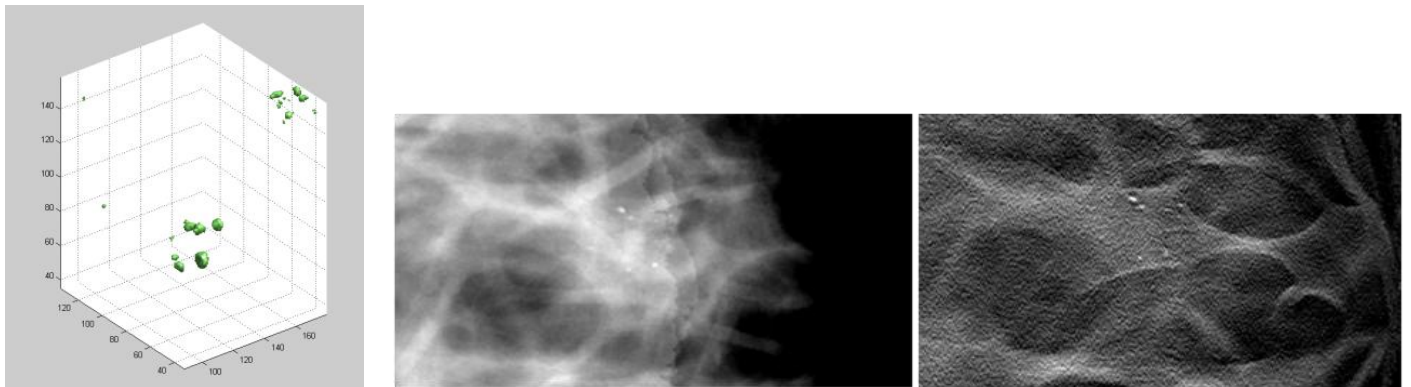
Figure 10 (a) An example of a malignant a calcification cluster extracted from clinical images. Details of synthetic images of a phantom with an embedded cluster: (b) DM; and (c) a reconstructed DBT image.
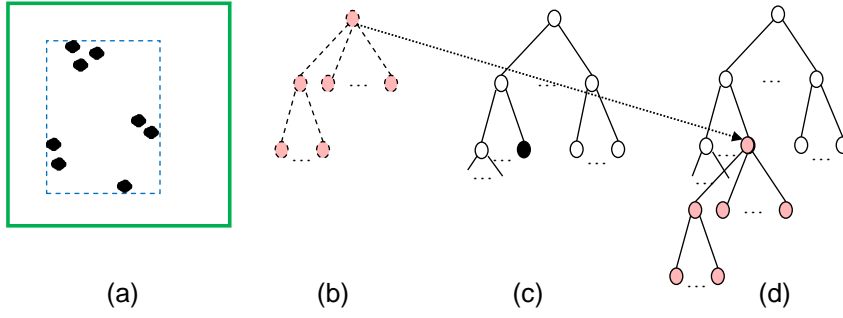
Figure 11 (a) 2D illustration of a calcification cluster binary image (black circles), minimal bounding rectangle (dashed) and the sub-volume corresponding to an octree node of the phantom (bold); (b) Octree corresponding to the cluster; (c) The selected phantom node for cluster placement (black circle); (d) Octree of the phantom with the cluster after insertion.

We have compared two methods for simulation of dense tissue distribution in a software breast phantom: (1) the previously used Gaussian distribution centered at the phantom nipple point, and (2) the combination of two Beta functions, one modeling the dense tissue distribution along the chest wall-to-nipple direction, and the other modeling the radial distribution in each coronal section of the phantom, see Figure 12. Dense tissue distributions obtained using these methods have been compared with distributions reported in the literature estimated from the analysis of breast CT images. Qualitatively, the two methods produced rather similar dense tissue distributions. The simulation based upon the use of Beta functions provides more control over the simulated distributions through the selection of the various Beta function parameters. Both methods showed good agreement to the clinical data, suggesting both provide a high level of realism, see Figure 13. Preliminary results have been published in [Chui et al., SPIE 2013; listed in Section 4 as Ref. #4].
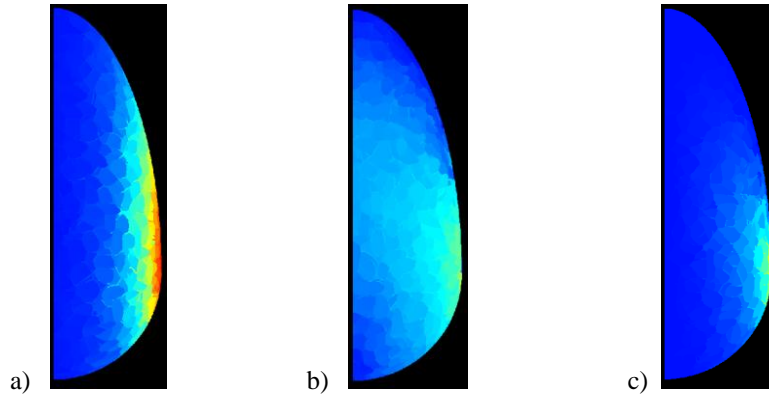

Figure 12 Probability maps of compartments labeled as dense tissues: a) Gaussian b) Beta1 and c) Beta 2.
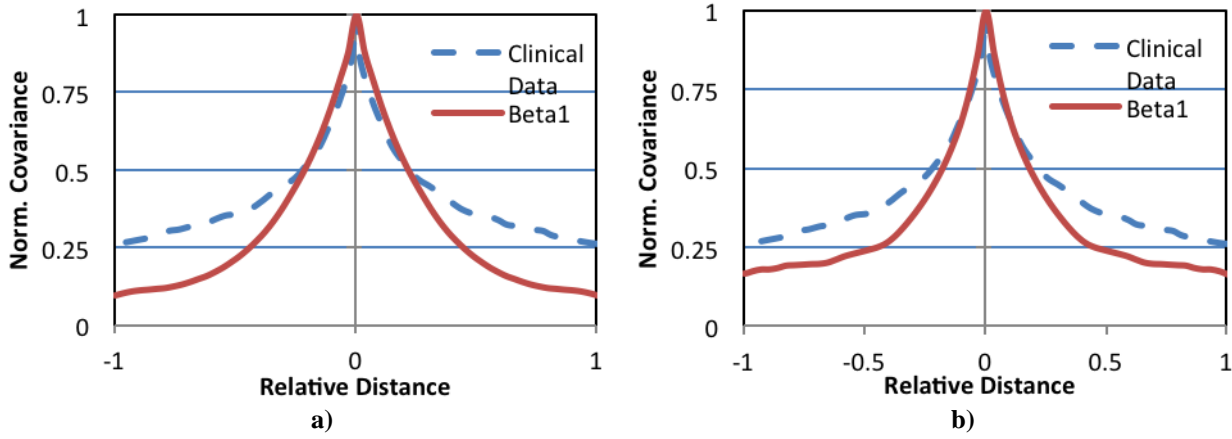
Figure 13 Profiles of average normalized covariance matrices in a) posterior-to-anterior direction; and b) top-to-bottom direction from simulated data created with Beta1 method and clinical data (modified from Freed et al. [11]). FWHMs measured from clinical data are 0.450(posterior-to-anterior) and 0.466 (top-to-bottom). FWHMs measured from simulated data using Beta1 are 0.433 (posterior-to-anterior) and 0.366 (top-to-bottom).

Further modification to our simulation algorithm is proposed, in order to improve the quality of simulated projections generated using software breast phantoms. Anthropomorphic software breast phantoms have been used for quantitative validation of breast imaging systems. Previously, we developed a novel algorithm for breast anatomy simulation, which did not account for the partial volume (PV) of various tissues in a voxel, see Figure 14; instead, each phantom voxel was assumed to contain single tissue type. As a result, phantom projection images displayed notable artifacts near the borders between regions of different materials, particularly at the skin-air boundary. These artifacts diminished the realism of phantom images. One solution is to simulate smaller voxels. Reducing voxel size, however, extends the phantom generation time and increases memory requirements. We achieved an improvement in image quality without reducing voxel size by the simulation of PV in voxels containing more than one simulated tissue type, see Figure 15. The linear x-ray attenuation coefficient of each voxel is calculated by combining attenuation coefficients proportional to the voxel subvolumes occupied by the various tissues. A local planar approximation of the boundary surface is employed, see Figure 16, and the partial volume in each voxel is computed by decomposition into simple geometric shapes.
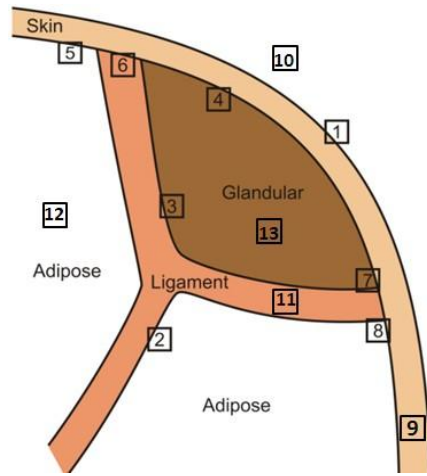
Figure 14 Possible cases of voxels containing multiple materials (partial volume voxels) in a breast phantom.

(a)	(b)	(c)	(d)
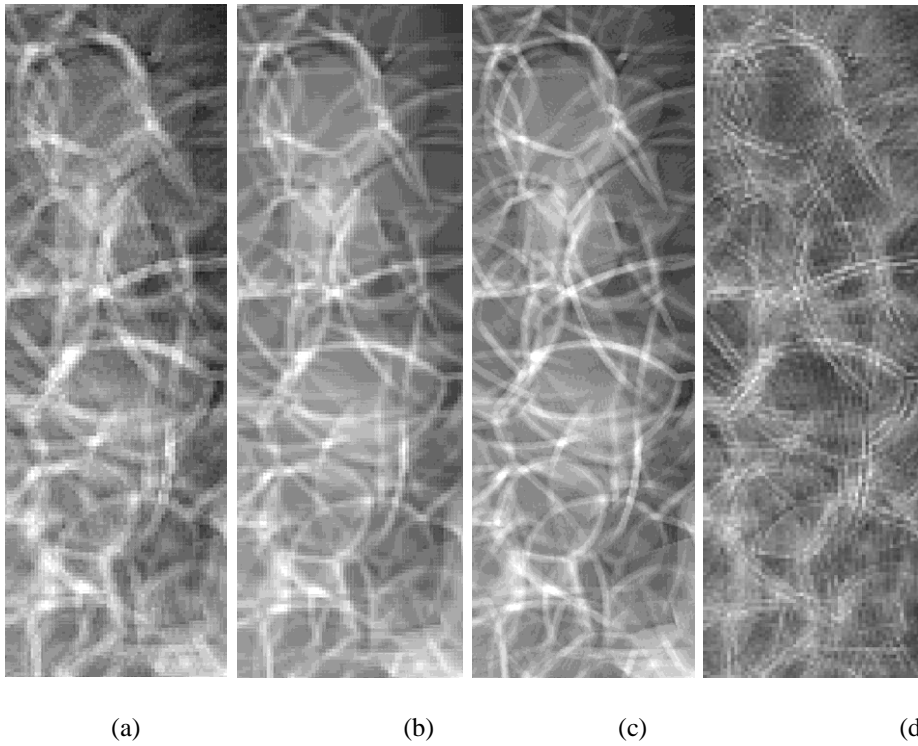
Figure 15 Simulated projections of (a) a phantom with 400μm voxels and no PV; (b) the phantom from (a) with simulated PV; and (c) the same phantom generated at 200 μm voxels and no PV. (d) The difference between (a) and (b); the image contrast was enhanced for display purposes.
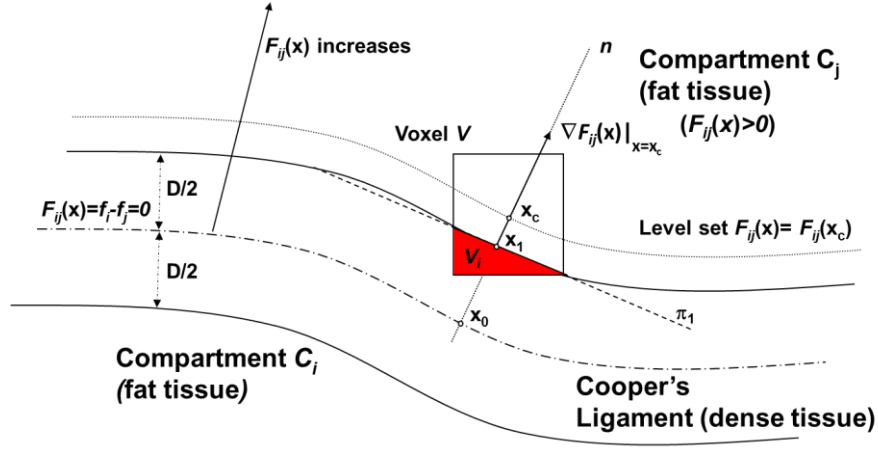
Figure 16 Planar approximation of a boundary between Cooper's ligament and a compartment.

An efficient encoding scheme is proposed for the type and proportion of simulated tissues in each voxel, see Table 1.

Table 1: Taxonomy of voxels in the phantom and encoding in the phantom.

| Case	p_1 (6 bits)	p_2 (6 bits)	Label (4 bits)
1. Skin	0	0	0
2. Air	0	100	0
3. Cooper's ligament	0	0	1
4. Fat	0	0	2
5. Dense	0	0	3
6. Skin; air	0	p_{Air}	0
7. Skin; fat tissue	0	p_{Skin}	2
8. Skin; dense tissue	0	p_{Skin}	3
9. Skin; Cooper's ligament	p_{Cooper}	0	0
10. Cooper's ligament; fat	p_{Fat}	0	1
11. Cooper's ligament; dense	0	p_{Dense}	1
12. Skin, Cooper's ligament and fat tissue	p_{Cooper}	p_{Skin}	2
13. Skin, Cooper's ligament and dense tissue	p_{Cooper}	p_{Skin}	3

We designed and implemented algorithm for a general case for simulation of the partial volume (PV) of voxels containing up to three materials, Figure 17 (published in Chen et al., SPIE 2012 and Chen et al., IWDM 2012; listed in Section 4 as Refs. #2 and #3).
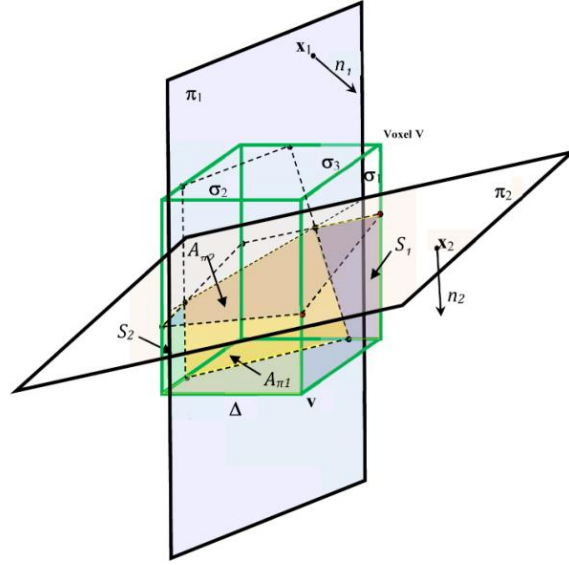
Figure 17 Partial volume V_i of the voxel V above planes π_1 and π_2 and containing vertex **v**. S_1, S_2 and S_3(here S_3=0) are surface areas of parts of the volume boundary belonging to voxel sides σ_1, σ_2 and σ_3 that do not contain the vertex **v**.

We developed a method for validation of partial volume computation based on the Monte Carlo simulation and demonstrated that the accuracy of the computation is close to one determined by the discretization error. We also studied computation of partial volumes based on the Monte Carlo and developed technique to determine the parameters of the Monte Carlo simulation in order to achieve a specified accuracy.

We worked on improving linear approximation of the distance between a voxel and the surface of the Cooper's ligaments. We derived an exact formula for the gradient of the surface of the ligament. The preliminary results demonstrated improvements in computed partial volumes due to utilization of the improved linear approximation.

We developed a highly-parallel implementation of the algorithm based on GPU architecture in order to reduce the time needed to generate software breast phantoms. The rapid generation of high resolution phantoms is needed to support virtual clinical trials of breast imaging systems. We compared the performance of GPU implementation with the single- and multi-threaded CPU C/C++ implementation and observed significant speedups, see Figure18 which made it possible to generate phantoms at the resolutions of 12.5 μm. The results of the parallel implementation have been published in [Chui et al., SPIE 2012 and Chui et al., IWDM 2012; listed in Section 4 as Refs. #1 and #5].
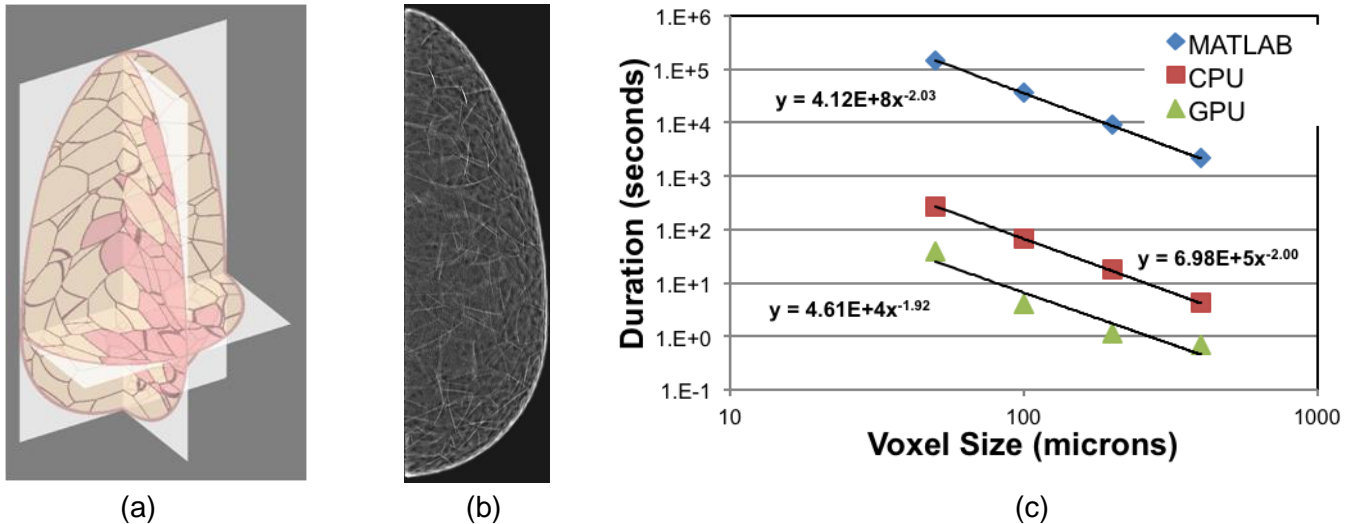
Figure 18 (a) Cross-sections of a simulated 25μm phantom; (b) Projection of a simulated 200μm phantom; (c) Average simulation times expressed as a function of voxel size for different implementations of the octree-based algorithm.

We worked on theoretical properties of the proposed oct-tree based recursive partitioning simulation algorithm. Currently, we are working on proving its quadratic computational complexity and asymptotic optimality using the fractal theory.

- Prepare peer-review publications on the results of the proposed research. (Y3-Y4)

While working on the current research, we have prepared several publications about our results. These publications are listed in the section on "Reportable Outcomes".

- Validate success of the research training program by annual teleconferences with and bi-annual visits by external Advisory Committee.

DSU faculty had by-monthly teleconference during 2012 year. The teleconferences will be continued in 2013.

Our collaborative work (particularly during Dr. Pokrajac's sabbatical leave from DSU to work with Dr. Maidment and Dr. Bakic in Fall semester of 2011) generated an NIH R01 grant proposal in Spring 2012 to the RFA on the Continued Development of Biomedical Software (PAR-11-028).

2.3 Objective 3

Produce a corpus of high-quality published work and develop a portfolio of independently funded research grants at DSU to support a sustained breast cancer program

- See Reportable outcomes for publications

- In June 2012, we submitted an NIH R01 grant proposal to the RFA on the Continued Development of Biomedical Software (**PAR-11-028):** http://grants.nih.gov/grants/guide/pa-files/PAR-11-028.html), P. Bakic, D. Pokrajac, A. Maidment, entitled "Continued Development and Maintenance of Computer Simulation of Breast Anatomy". The proposal was scored at 41%. We plan to resubmitted in July 2013.

3. Important Findings

- We finalized ACRIN data transfer on MIRC and resolved issues with various batch transfers;

- We performed a preliminary query of the ACRIN data aimed at identifying the prevalence of women with incomplete visualization of the breast;

- We developed a code to estimate the breast cancer risks using the demographic metadata information from the ACRIN cases;

- We estimated breast densities for GE mammograms from the ACRIN database, using the software developed at the University of Pennsylvania;

- A novel breast image registration method is proposed to obtain a composite mammogram from several images with partial breast coverage, for the purpose of accurate breast density estimation;

- We developed and validated several modifications and novel features to breast anatomy simulation methods, used for generating software breast phantoms, including: (1) a method to improve thickness control of the Cooper's ligaments in the simulation algorithm by reducing "dents" on the ligaments' surface; (2) a method for insertion of simulated microcalcification clusters in the software breast phantom; (3) a method for simulating the dense tissue distribution in the software phantom; and (4) a method for reducing quantization artifacts in phantom images by simulating partial volume in voxels containing several simulated tissue types. The listed novel features have resulted in further improvement of the image quality in synthetic breast images generated using the software phantom.

4. Reportable Outcomes

Publications (journal papers and conference proceedings):

1. J. Chu, D. Pokrajac, A. D. Maidment, P. Bakic, "Toward Breast Anatomy Simulation using GPU," Proc. Breast Imaging (IWDM), Lecture Notes in Computer Science 7361, pp. 508-515, 2012.

2. F. Chen, D. Pokrajac, X. Shi, F. Liu, A. D. Maidment, P. Bakic, "Simulation of Three Materials Partial VolumeAveraging in a Software Breast Phantom," Proc. Breast Imaging (IWDM), Lecture Notes in Computer Science 7361, pp. 151-158, 2012.

3. F. Chen, P. Zheng, P. Xu, D. Pokrajac, P. R. Bakic, Andrew D. A. Maidment, F. Liu, X. Shi, "Breast image registration by using non-linear local affine transformation," Proc. of SPIE 8668, in press.

4. J. Chui, R. Zeng, D. Pokrajac, S. Park, K. J. Myers, A. D. A. Maidment, P. R. Bakic, "Two methods for simulation of dense tissue distribution in software breast phantoms," Proc. of SPIE 8668, in press.

5. Chui, J.H., Pokrajac, D.D., Maidment, A.D.A., Bakic, P.R.: "Roadmap for Efficient Parallelization of Breast Anatomy Simulation," In Physics of Medical Imaging, Proc. SPIE 8313, edited by N.J. Pelc, R.M. Nishikawa 2012.

Presentations:

1. D. Pokrajac made a presentation at the IWDM 2012, the 11th International Workshop on Breast Imaging, in Philadelphia, PA. on July 8-11, 2012, "Toward Breast Anatomy Simulation using GPU" (co-authored by J. Chu, D. Pokrajac, A. D. Maidment, P. Bakic)

2. F. Chen made a presentation at the IWDM 2012, the 11th International Workshop on Breast Imaging, in Philadelphia, PA. On July 8-11, 2012, "Simulation of Three Materials Partial Volume Averaging in a Software Breast Phantom" (co-authored by F. Chen, **D. Pokrajac**, X. Shi, F. Liu, A. D. Maidment, P. Bakic)

Grant Applications:

- Submitted an NIH R01 grant proposal to the RFA on the Continued Development of Biomedical Software (**PAR-11-028**): http://grants.nih.gov/grants/guide/pa-files/PAR-11-028.html) P. Bakic, D. Pokrajac, A. Maidment. Grant scored at 41 percentile, not funded. Resubmission for July 2013 in preparation.

5. Conclusion

This year we submitted an NIH R01 grant proposal to the RFA. We organized DSUPENN seminars, attended and presented at national and international conferences. We held by-monthly teleconferences with DSU and UPENN. We finalized ACRIN data transfer on MIRC and resolved issues with various batch transfers. We performed a preliminary query of the ACRIN data aimed at identifying the prevalence of women with incomplete visualization of the breast. We developed a code to estimate the breast cancer risks using the demographic metadata information from the ACRIN cases. We estimated breast densities for GE mammograms from the ACRIN database, using the software developed at the University of Pennsylvania. A novel breast image registration method is proposed to obtain a composite mammogram from several images with partial

breast coverage, for the purpose of accurate breast density estimation. We designed a method to improve thickness control of the Cooper's ligaments in the simulation algorithm by reducing "dents" on the ligaments' surface.

6. References

N/A

7. Appendices

1. J. Chu, D. Pokrajac, A. D. Maidment, P. Bakic, "Toward Breast Anatomy Simulation using GPU," Proc. Breast Imaging (IWDM), Lecture Notes in Computer Science 7361, pp. 508-515, 2012.

2. F. Chen, D. Pokrajac, X. Shi, F. Liu, A. D. Maidment, P. Bakic, "Simulation of Three Materials Partial Volume Averaging in a Software Breast Phantom," Proc. Breast Imaging (IWDM), Lecture Notes in Computer Science 7361, pp. 151-158, 2012.

3. F. Chen, P. Zheng, P. Xu, D. Pokrajac, P. R. Bakic, Andrew D. A. Maidment, F. Liu, X. Shi, "Breast image registration by using non-linear local affine transformation," Proc. of SPIE 8668, in press.

4. J. Chui, R. Zeng, D. Pokrajac, S. Park, K. J. Myers, A. D. A. Maidment, P. R. Bakic, "Two methods for simulation of dense tissue distribution in software breast phantoms," Proc. of SPIE 8668, in press.

Towards Breast Anatomy Simulation Using GPUs

Joseph H. Chui[1], David D. Pokrajac[2],
Andrew D.A. Maidment[3], and Predrag R. Bakic[4]

[1] Department of Radiology, University of Pennsylvania, Philadelphia PA 19104
{Joseph.Chui,Andrew.Maidment,Predrag.Bakic}@uphs.upenn.edu
[2] Applied Mathematics Research Center, Delaware State University, Dover, DE 19901
dpokrajac@desu.edu

Abstract. We have developed a method for massively parallelized breast anatomy simulation and a corresponding GPU implementation using OpenCL. The simulation method utilizes an octree data structure for recursively splitting the simulated tissue volume. Several strategies to optimize the GPU utilization were proposed and evaluated, including the use of synchronization constructs in the language and minimization of buffer allocations. The task of tissue classification was separated from the voxelization to further improve the balance of the control flow. The proposed anatomy simulation method provides for fast generation of high-resolution anthropomorphic breast phantoms. Currently, it is possible to generate an octree representation of 450 ml breasts with 50 μm voxel size on a AMD Radeon 6950 GPU with 2GB of memory at a rate of 7 phantoms per minute, 32 times faster than a multithreaded C++ implementation.

Keywords: Digital mammography, anthropomorphic breast phantom, Parallelization, GPU.

1   Introduction

Breast tissue simulation is of great importance for pre-clinical testing and optimization of imaging systems or image analysis methods. Currently, the standard for imaging systems validation includes pre-clinical evaluation performed with simple geometric phantoms, followed up by clinical imaging trials involving large numbers of patients and repeated imaging using different acquisition conditions. Such an approach frequently causes delays in technology dissemination, due to the duration and cost of these trials. In addition, there are many factors which place strict limitations on the number of test conditions, such as the use of radiation in x-ray imaging trials.

Use of software anthropomorphic phantoms for pre-clinical evaluations offers a valuable alternative approach which can reduce the burden of clinical trials. In this paper, we present a GPU (Graphical Processing Unit) implementation of a method for generating software anthropomorphic breast phantoms. The breast anatomy simulation method is based upon recursive partitioning of the simulated volume utilizing octrees. The octree-based algorithm allows generation and processing of octree nodes at the same tree level independently (i.e., in any arbitrary order), which makes the

algorithm a good candidate for parallelization.   Using profiler analysis we have identified the bottleneck steps in the CPU implementation of the algorithm and developed a corresponding GPU implementation using OpenCL. The performances of the GPU and CPU implementations were compared in terms of the time needed for generating phantoms of various voxel sizes. The effects of several implementation parameters are discussed.

2   Methods

Our proposed method of breast anatomy simulation using GPUs is based on the algorithm originally proposed by Pokrajac et al [1]. The paper proposed a method of using octrees to represent simulated volumes of various tissue types. We recently proposed a roadmap [2] to migrate its implementation to a platform that directly utilizes massively parallel processors such as GPUs. Specific milestones were defined to allow incremental migration in implementations and regression testing. A multiple threaded, concurrent version targeting multiple-core CPUs had been implemented along the roadmap. Figure 1 shows the flowchart of this version of algorithm.
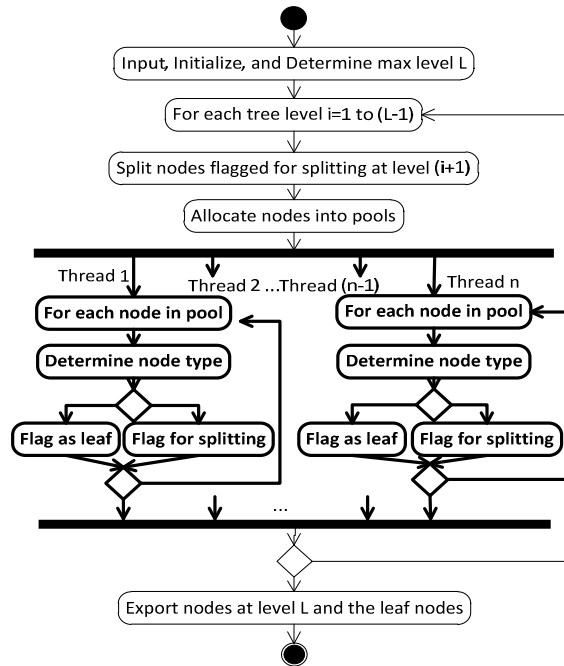
Fig. 1. Flowchart of the concurrent version of the octree-based algorithm, where nodes are processed concurrently to determine their tissue types

We chose OpenCL [3] as our software platform to implement a massively parallel version of the algorithm. Each individual octree node is identified as the finest granularity in the parallelization. To map it to OpenCL, each OpenCL work item is indexed to a unique node at each tree level. The concurrent part of the algorithm is ported into OpenCL kernels which are functions invoked and executed by the GPUs.

Profiling was performed on the initial OpenCL implementation to identify its potential bottlenecks using AMD APP SDK v2.6 [4]. The data transfer between the host memory and the device memory was identified as the major bottleneck in the pipeline. To reduce the amount of data transferred between the host and the devices, the process of splitting the nodes into child nodes was ported as an OpenCL kernel, so that the uploading of octree data to the devices was no longer needed. Figure 2 shows a float chart where the node splitting is parallelized on the GPU.
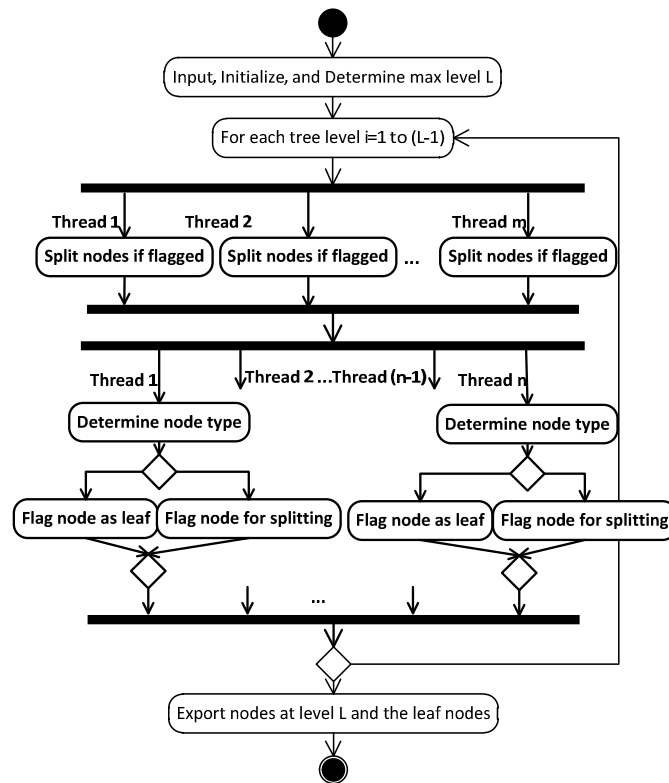
Fig. 2. A massively parallel version of the octree algorithm. At each octree level, two parallelized steps are performed. The first step is to split each splitable node into 8 child nodes. The second step is determining the tissue type of each node.

Because OpenCL does not allow allocation of memory by its kernels, buffers of sufficient sizes have to be allocated by the host in advance. Therefore, the GPU implementation has to determine, in advance, the number of octree nodes requiring for splitting. A technique similar to reduction [5] is used to accelerate the counting

process. The implementation first counts the number of nodes which require splitting in each work group using a counter in local memory. Next, the counts of each workgroup are accumulated so that the accumulation result multiplied by 8 would be the index where each workgroup starts splitting its nodes in parallel. Figure 3 shows an example of the parallelized splitting process.
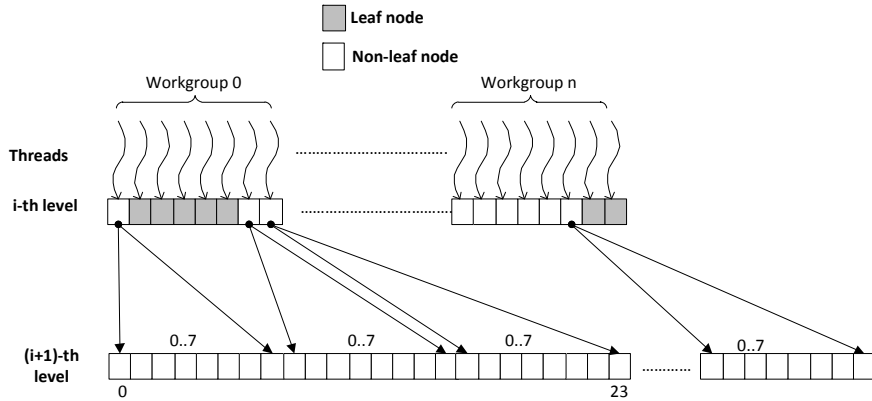
Fig. 3. Illustration of GPU threads splitting its each node into eight nodes in parallel. In this example, workgroup 0 has 3 nodes (0, 6, and 7) requiring splitting. Indexes 0 to 23 (= 3 x 8 - 1) are reserved for workgroup 0, while the next workgroup splits the nodes into child nodes starting from index 24.

Built-in OpenCL atomic functions `atom_inc()` and `atom_add()` were utilized to increment and add the counters on multiple threads to guard against a race condition.

During software profiling, several other GPU-specific bottlenecks were also identified. First, buffer allocations on GPUs require significant time. Secondly, excessive use of flow control in the kernels running on the GPUs slows down the execution of work groups.

To address the buffer allocation problem, instead of re-allocating new buffers for every level of octrees, buffers were retained on the devices until the current ones were no longer big enough for the next tree level. This was especially effective for phantoms of high resolution, where the buffers created for an octree section could often be reused for subsequent sections.

To tackle the issue of excessive use of flow control, the OpenCL kernels implemented in this study were refactored manually. Programming methods using branching that are designed for sequential computation are often unsuitable for parallel computation [6]. Instead, costly functions called on different control paths can be consolidated into a single call on the main path.

Our concurrent, non-parallel version of the algorithm conditionally voxelizes volumes on some of its control paths based on each node's tissue types. The whole workgroup is blocked when there is a work item in this group requires voxelization of

its octree node. To improve the utilization of the GPU, the voxelization was separated from the kernel that determines each node's tissue type.

We validated the implementation by comparing the generated octrees with the ones generated by previous implementations using the same set of parameters. In order to assess the performances of various implementations, the simulation times at different target resolutions were compared. We also measured the effects of workgroup sizes on the performance. Performances of the implementations were assessed by their duration times on a desktop PC with Intel® Core™ i7-2600K CPU @ 3.40GHz and 16GB of RAM and Radeon 6950 GPU with 2GB of VRAM.

3   Results

Figure 4 shows the orthogonal sections of a phantom with 400 μm and 50 μm voxel resolutions. With the same inputs, the identical octrees were constructed by the different implementations.
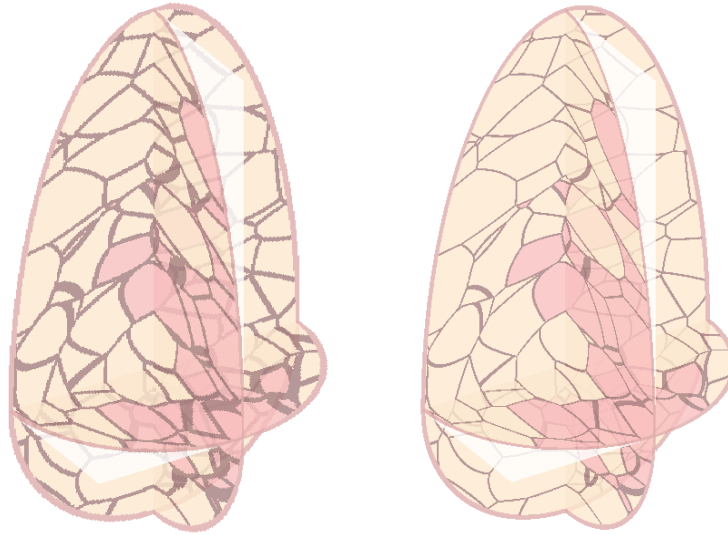

Fig. 4. Orthogonal sections of a simulated breast phantom of (a) 400μm and (b) 50μm resolutions

The performance of the OpenCL implementation was assessed by comparing the duration times to generate phantoms of various voxel sizes. The duration time of each configuration was measured by averaging the duration times of 5 independent phantoms; each phantom was generated from a different set of ellipsoids modeled randomly inside the simulated breast. Figure 5 is a graph showing the duration times of 2 implementations at different voxel resolutions. Figure 6 shows the duration times measured for 25μm resolution using different OpenCL workgroup sizes.
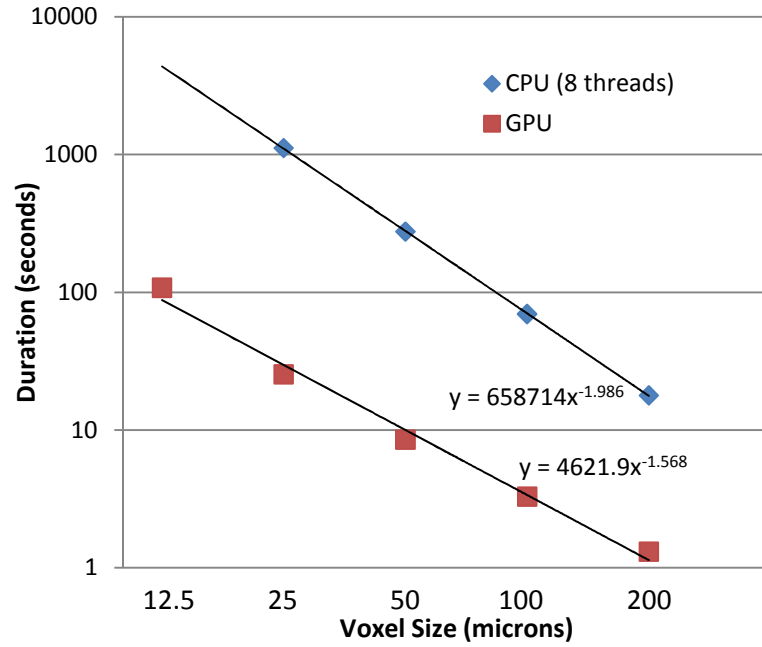
Fig. 5. Average duration times of different implementations of the octree-based algorithm for various voxel sizes (12.5, 25, 50, 100 and 200 μm)
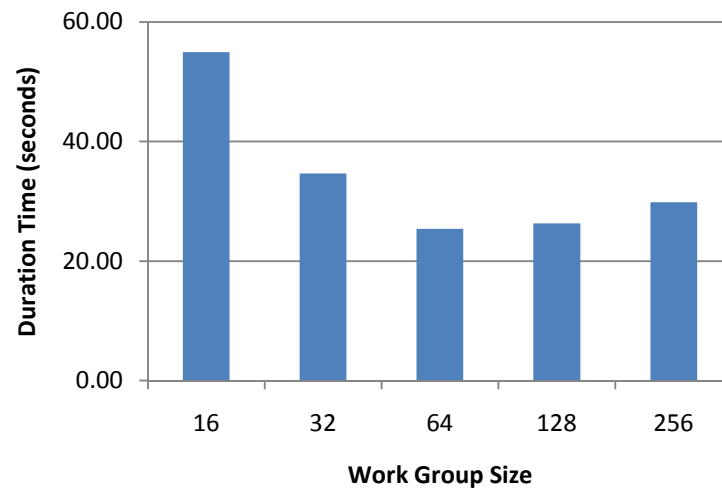
Fig. 6. The duration times using different OpenCL workgroup sizes (16, 32, 64, 128, and 256)

4   Discussion and Conclusions

We have successfully implemented an efficient parallelized version of an algorithm to simulate the breast anatomy for anthropomorphic phantoms by utilizing some of the strategies targeted for GPUs such as reuse of buffers and reduction of flow control. We measured, on average, a 32-fold improvement for the GPU implementation over the multi-threaded CPU implementation when simulating 50 μm phantoms.

Based on the measured duration times using different workgroup sizes, a workgroup of 64 yielded the best performance. Since the GPU used in this study has a wavefront size of 64 work items, any work group size less than 64 may underutilize the GPUs. On the other hand, a workgroup of more than 64 items would increase the memory contention among the units. Since the optimal workgroup size is hardware dependent, benchmarking on individual hardware is required to determine the optimal work group size.

The performance of the implementation is sufficient to create phantoms of reasonably high resolution in near real time. By generating and storing the data on the GPU, it becomes feasible to develop real time visualization software that interoperates with the same set of data on the GPU. This arises, in part, because the octree data structure offers a superior memory footprint compared to a 3D voxel representation. Therefore, an octree is an ideal data structure for storage on GPUs (that are typically available with limited memory). For simulations requiring higher resolution, the simulated phantom can be subdivided into sub-volumes small enough for the individual GPUs.

We observed a CPU usage of 2% by the application when the octrees are generated on the GPU. Thus, porting the code to the GPU not only resulted in the performance being significantly improved, but shifting the processing from the CPU to the GPU frees the CPU for other operations such as voxelization, data compression and I/O. Our GPU implementation can be further enhanced by operating it upon multiple GPUs; a feature supported by most mainstream performance computing hardware. It is noteworthy that it is more feasible to assemble hardware with multiple GPUs than hardware with multiple CPUs.

Our latest profiling results indicate that further improvements in performance can be achieved by extending the parallelization to the evaluation of shape functions for each octree. Please note that the estimated slope of the dependence of the computation time vs. voxel size for the GPU implementation (Fig. 5) is less than two. The computation time consists of two components. The first component, related to building and maintaining the octree structure of the phantom, is believed to be quadratic function of the inverse voxel size [1]. The second component includes overhead of initializing the OpenCL kernels that has linear or constant complexity as a function of the inverse voxel size. For larger voxel sizes, this linear component becomes dominant, influencing the estimate slope of the regression line.

It is further observed that when the resolution is sufficiently high, the duration increased slightly more than a quadratic as a function of the inverse voxel size. This is caused mainly by the overhead of the data transfers between the host and the devices, which accrue a cost proportional to the cube of the inverse voxel size. For simulations that require resolutions higher than 25 μm, further investigations of performance

improvement are needed. Such work should emphasize the reduction of the cost of operations for each sub-volume, such as voxelization and communication between the host and devices. Finally, the frequency of buffer allocation on the devices can be reduced if an accurate maximum buffer size can be estimated in advance for different sets of parameters.

References

1. Pokrajac, D.D., Maidment, A.D.A., Bakic, P.R.: Optimized generation of high resolution breast anthropomorphic software phantoms. Medical Physics 39(4), 2290–2302 (2012)
2. Chui, J.H., Pokrajac, D.D., Maidment, A.D.A., Bakic, P.R.: Roadmap for efficient parallelization of breast anatomy simulation. In: Pelc, N.J., Nishikawa, R.M., Whiting, B.R. (eds.) Proc. of SPIE, Medical Imaging 2012: Physics of Medical Imaging, vol. 8313, pp. 83134T-1–83134T-10, SPIE, Bellingham (2012)
3. OpenCL 1.2 Specification, Khronos Group,
   `http://www.khronos.org/registry/cl/specs/opencl-1.2.pdf`
4. AMD APP SDK v2.6,
   `http://developer.amd.com/sdks/AMDAPPSDK/downloads/Pages/`
   `default.aspx`
5. Harris, M.: Optimizing parallel reduction in CUDA,
   `http://developer.download.nvidia.com/compute/cuda/1_1/`
   `Website/projects/reduction/doc/reduction.pdf`
6. AMD Accelerated Parallel Processing OpenCL Programming Guide (v1.3f),
   `http://developer.amd.com/sdks/AMDAPPSDK/assets/`
   `AMD_Accelerated_Parallel_Processing_OpenCL_`
   `Programming_Guide.pdf`

Simulation of Three Material Partial Volume Averaging in a Software Breast Phantom

Feiyu Chen[1], David D. Pokrajac[1], Xiquan Shi[1], Fengshan Liu[1], Andrew D.A. Maidment[2], Predrag R. Bakic[2]

[1]Delaware State University, 1200 N DuPont Hwy, Dover DE 19904;
`FChen09@students.desu.edu;{DPokrajac,XShi,FLiu}@desu.edu;`

[2]University of Pennsylvania, 3400 Spruce Street, Philadelphia, PA 19104
`{Predrag.Bakic,Andrew.Maidment}@uphs.upenn.edu`

Abstract. A general case for simulation of partial volume (PV) averaging in software breast phantoms is presented. PV simulation could improve the quality of phantom images by reducing quantization artifacts near borders between different materials. The validity of phantom studies depends on the realism of simulated images, which is affected by the size of phantom voxels. Large voxels may cause notable quantization artifacts; small voxels, however, extend the generation time and increase the memory requirements. An improvement in image quality without reducing voxel size is achievable by the simulation of PV averaging in voxels containing more than one simulated tissue type; the linear x-ray attenuation coefficient of such voxels is represented by a combination of attenuation coefficients proportional to voxel subvolumes occupied by different tissues. In this paper, we present results of simulated PV in the general case of voxels containing up to three materials.

Keywords: Digital mammography, computer breast phantom, partial volume simulation, computational geometry.

1   Introduction

This study is motivated by the desire to improve the quality of synthetic images generated using software breast phantoms. The partial volume (PV) averaging can help reduce the quantization artifacts on boundaries of regions with different simulated materials. The software phantoms in this study have been generated based upon the recursive partitioning of the phantom volume using octrees [1]. In this paper, we propose a solution for a general PV case with up to three simulated materials in a voxel. This work represents the first PV simulation in software phantoms generated based upon the rules for simulating anatomical structures [1-4]. PV simulation has been indirectly reported in a method for generating phantoms based upon the CT images of mastectomy specimen [5]. In that method, the values of each reconstructed breast CT image voxel were scaled and interpreted as the percentage of adipose breast tissue in the voxel.

In this paper, we present an overview of the PV simulation method including details of a planar approximation and the PV computation. The improvement of image quality is qualitatively validated. The results are shown in the form of slices and simulated X-ray projections of phantoms with and without PV.

2   Method

The effective linear x-ray attenuation in a voxel which contains more than one simulated material can be calculated as:

$$\mu_v = \frac{1}{|V|}\sum_i \mu_i |V_i| = \sum_i \mu_i p_i ; \ \ p_i = \frac{|V_i|}{|V|}\times 100\% ,$$ (1)

where $|V|$ is the voxel volume, $|V_i|$ is the subvolume of material i with the linear x-ray attenuation μ_i, and p_i is the percentage of the material i in the voxel (Fig. 1a). One can distinguish the following cases of PV (Fig 1b):

A. *Two materials with one bounding surface*: (1) Skin and air; (2) Cooper's ligament and adipose tissue; (3) Ligament and fibroglandular dense tissue; (4) Skin and dense tissue; (5) Skin and adipose tissue, and (6) Skin and Cooper's ligament;

B. *Three materials with two bounding surfaces*: (7) Skin, ligament, and dense tissue; and (8) Skin, ligament, and adipose tissue

(a)   (b)
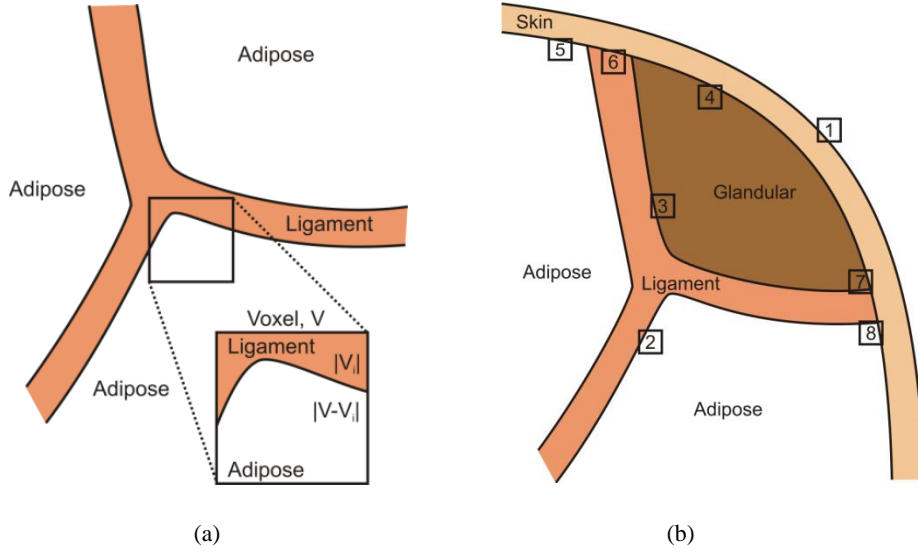
Fig. 1. (a) The concept of PV simulation; V denotes the voxel volume and V_i is the sub-volume occupied by dense tissue.(b) Different cases of material combination in a voxel.
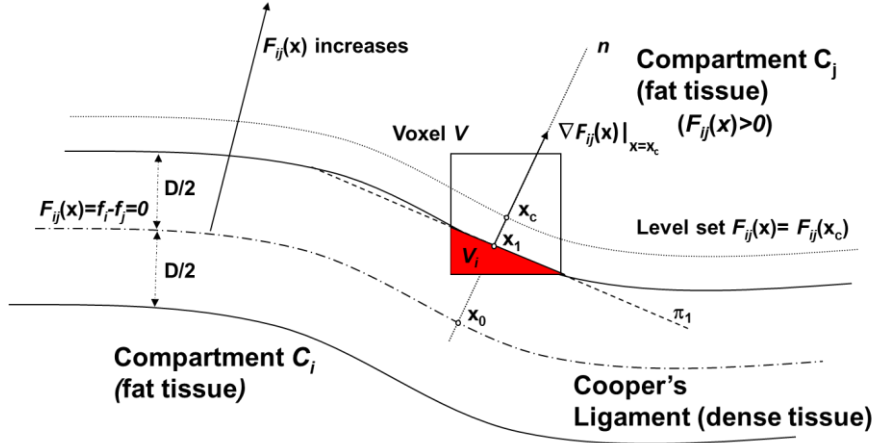
The simulation of PV case (1) has been reported previously [6]; it can be easily extended to cases (2)-(6). In this abstract we present a general case of PV simulation based upon the planar approximation of up to two bounding surfaces in a voxel, addressing cases (7)-(8).

The planar approximation for the boundary between Cooper's ligaments and adipose tissue, as simulated in our software breast phantom [1], can be obtained as follows. Adipose compartments C_i and C_j, which may be given by shape functions f_i and f_j, determine a Cooper's ligament between them as the locus of points within a distance of D/2 from a surface $F_{ij}(\mathbf{x}) = f_i(\mathbf{x}) - f_j(\mathbf{x})$, see Fig. 2. Consider a voxel V with center $\mathbf{x}_c$. We define a planar approximation π_1 of the boundary between the Cooper's ligament and the compartment C_j as

$$\pi_1 : \left(\mathbf{x} - \mathbf{x}_1\right) \cdot sign\!\left(F_{ij}\!\left(\mathbf{x}_c\right)\right)\!\nabla F_{ij}\!\left(\mathbf{x}_c\right) = 0 , \qquad (2)$$

where

$$\mathbf{x}_1 = \mathbf{x}_c + sign\!\left(F_{ij}\!\left(\mathbf{x}_c\right)\right)\!\left(\mathrm{D}/2 - \frac{F_{ij}\!\left(\mathbf{x}_c\right)}{\left\|\nabla F_{ij}\!\left(\mathbf{x}_c\right)\right\|}\right)\!\frac{\nabla F_{ij}\!\left(\mathbf{x}_c\right)}{\left\|\nabla F_{ij}\!\left(\mathbf{x}_c\right)\right\|} . \qquad (3)$$

Fig. 2. Planar approximation of a boundary between Cooper's ligament and a compartment.

In a general PV case with three simulated materials and two bounding surfaces in a voxel, we can construct a planar approximation for each bounding surface (Fig. 3). The result of the approximation are planes $\pi_1 : (\mathbf{x} - \mathbf{x}_1)\hat{\mathbf{n}}_1 = 0$ and $\pi_2 : (\mathbf{x} - \mathbf{x}_2)\hat{\mathbf{n}}_1 = 0$. The partial volumes $|V_i|$ of interest are subsequently calculated as the volume of a portion of the voxel V (with center $\mathbf{x}_c$) that is bellow/above the planes. For example, the PV V_i corresponding to the fat tissue in Figure 4 is computed as a volume of a part of the voxel that is both above planes π_1 and π_2.

The PV V_i in a voxel shown in Fig. 3 has been computed using planar approximations as follows. Consider a voxel of linear size Δx, with a vertex **v** located above planes π_1 and π_2. (If no such vertex exists, the PV should be zero).
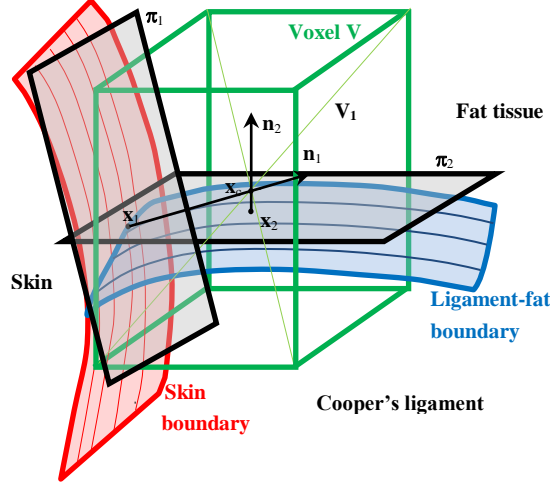
Fig. 3. A voxel containing skin, Cooper's ligament and fat tissue and planar approximations π_1 and π_2 of the tissue boundaries.

The divergence (or Gauss-Ostrogradsky) theorem [7] is employed to compute the partial volume $|V_i|$ of the voxel above planes π_1 and π_2, where the volume V_i is bounded by planes π_1 and π_2 and at most 6 sides of the voxel. The divergence theorem can be described as the following integral equation:

$$\iiint_{V_i} (\nabla \cdot F)dV = \oiint_S (F \cdot \mathbf{n})dS .\qquad (4)$$

The left side is a volume integral over the partial volume V_i of voxel, the right side is the surface integral over the boundary of the volume V_i, and n is the outward pointing unit normal vector of the boundary.

After the appropriate choice of the vector field function inside the integral at left side, *i.e.,* $F(\mathbf{x}) = \mathbf{x}$, the whole quantity at the left side becomes $3|V_i|$, and the right side can be rewritten as:
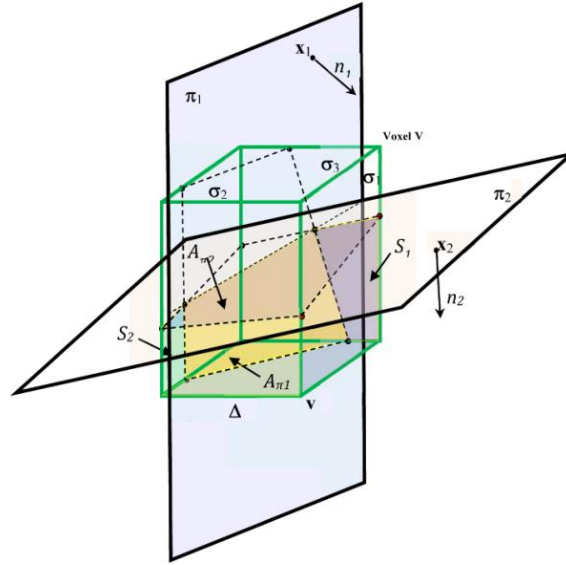
$$(S_1 + S_2 + S_3)\Delta x + A_{\pi 1}d_1 + A_{\pi 2}d_2 ,\qquad (5)$$

where S_i, $i=1,3$ are surface areas of the boundary formed by the voxel sides σ_1, σ_2 and σ_3, that do not contain the vertex **v**; $A_{\pi 1}$ and $A_{\pi 2}$ are surface areas of the boundary of V_i belonging to planes π_1 and π_2.

Subsequently, the PV can be calculated as:

$$|V_i| = \frac{(S_1 + S_2 + S_3)\Delta x + A_{\pi 1}d_1 + A_{\pi 2}d_2}{3} \, , \qquad (6)$$

where $d_1 = (\mathbf{v} - \mathbf{x}_1)\hat{\mathbf{n}}_1$, and $d_2 = (\mathbf{v} - \mathbf{x}_2)\hat{\mathbf{n}}_2$ are distances of the vertex $\mathbf{v}$ to planes π_1 and π_2.


Fig. 4. Partial volume V_i of the voxel V above planes π_1 and π_2 and containing vertex $\mathbf{v}$. S_1, S_2 and S_3(here S_3=0) are surface areas of parts of the volume boundary belonging to voxel sides σ_1, σ_2 and σ_3 that do not contain the vertex $\mathbf{v}$.

3   Results and Discussion

Fig. 5 illustrates the PV simulation in a 450ml software breast phantom with 400µm voxels. Shown is the segmentation of phantom detail into air and voxels containing one, two or three materials. For the corresponding phantom detail, shown also are the equivalent linear x-ray attenuations, and percentages of ligament tissue and skin tissue.

Fig. 5 suggests that the PV simulation on the ligaments-fat boundary was qualitatively correct. The voxels containing two materials are detected at the boundaries of two materials (e.g., skin, compartment). Similarly, the three material voxels are detected where the skin meets Cooper's ligaments and a compartment. Fig. 5b indicates that the PV helped smooth the appearance of boundaries between regions with different x-ray attenuations. The computed percentages of ligament and skin tissues in a voxel (Figs. 5c, 5d) suggest the correctness of the applied algorithm. The voxels in the interior of skin/ligaments contain 100% of the corresponding tissues, while the percentages gradually decrease at the boundaries.
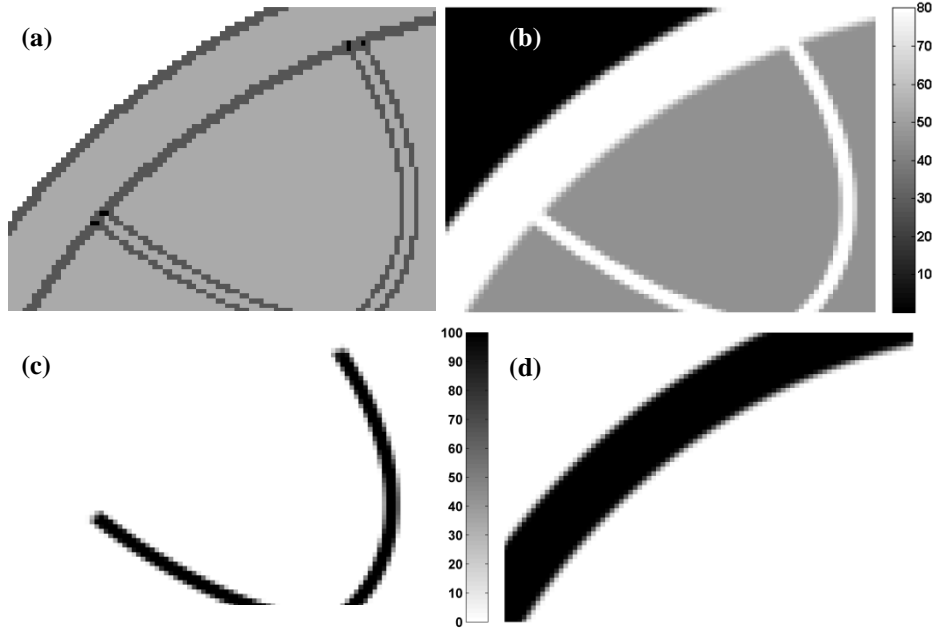
Fig. 5. Detail of a 450ml phantom with 400μm voxel size: (a) Segmentation of a phantom into air and voxels containing one (light gray), two (dark gray) or three (black) materials; (b) Simulated linear attenuation coefficients of voxels in (a) (in cm^{-1}, assuming monoenergetic x-ray beam at 20 keV); and percentage of (c) ligament tissue and (d) skin tissue in voxels from (a).

Fig. 6 shows simulated x-ray projections of phantoms with and without simulated PV. The simulated acquisition assumed a monoenergetic x-ray beam (at 20 keV) and parallel x-ray propagation, without scatter or quantum noise. The projections correspond to three phantoms with identical distributions of compartments: the phantom with 400μm voxels and no PV (Fig. 6a); the 400μm phantom with simulated PV (Fig. 6b); and the phantom with 200μm voxels and no PV (Fig. 6c). Shown also is the difference between the projections with and without simulated PV (Fig. 6d).

In a projection of the phantom with PV in Fig. 6b, the skin and Cooper's ligaments appear thinner (as compared to the phantom without PV, Fig. 6a). We believe this is caused by the reduction in the effective x-ray attenuations of voxels on the ligament/adipose tissue boundaries, which are lower than the x-ray attenuation of dense tissue (see Fig. 5b). Further, the characteristic stair-step quantization artifacts on tissue boundaries were noticeably reduced with simulated PV, as seen in the difference between PV and non PV projections (Fig 6d). Comparison of Figs. 6b and 6c indicates similar appearance of a phantom with PV simulated at a lower resolution (400μm) to a phantom simulated at a higher resolution (200μm) with no simulated PV. Hence, the application of PV may lead to an improvement in image quality without reducing voxel size.
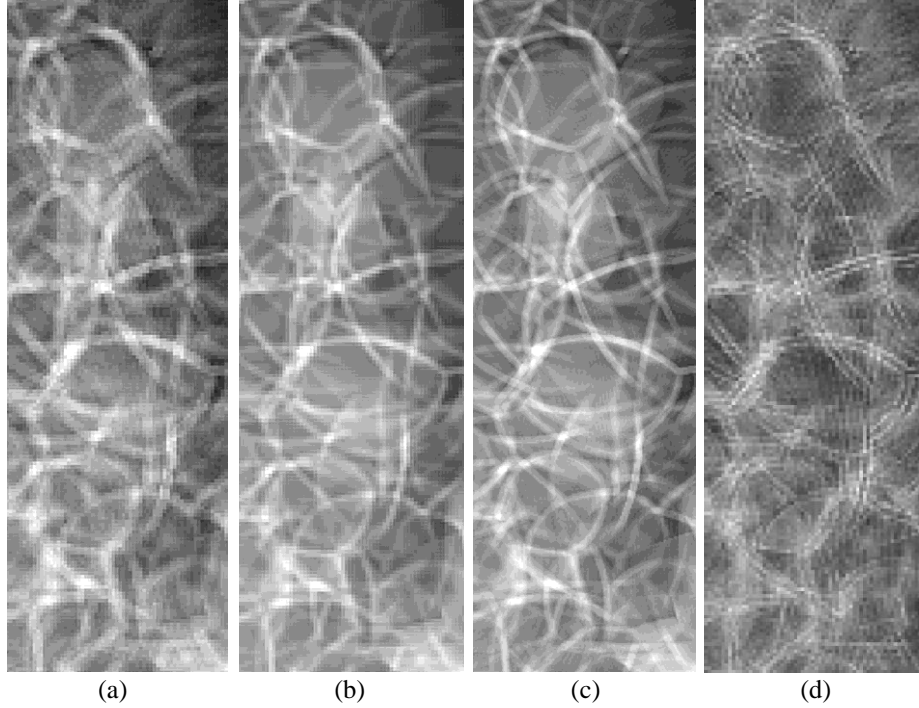
Fig. 6. Simulated projections of (a) a phantom with 400μm voxels and no PV; (b) the phantom from (a) with simulated PV; and (c) the same phantom generated at 200 μm voxels and no PV. (d) The difference between (a) and (b); the image contrast was enhanced for display purposes.

4   Conclusion

We have developed and qualitatively assessed a method for PV simulation of phantom voxels containing up to three simulated materials. The percentage of simulated tissues was estimated based upon the use of the Gauss-Ostrogradsky theorem. Cross-section and projections of phantoms with and without PV simulation were visually compared. PV simulation can improve the quality of phantom images by reducing the quantization artifacts caused by large voxel sizes.

References

1. D. D. Pokrajac, A. D. A. Maidment, and P. R. Bakic, "Optimized generation of high resolution breast anthropomorphic software phantoms," *Medical Physics*, vol. 39, pp. 2290-2302, 2012.
2. P. R. Bakic, C. Zhang, and A. D. A. Maidment, "Development and Characterization of an Anthropomorphic Breast Software Phantom Based upon Region-Growing Algorithm," *Medical Physics*, vol. 38, pp. 3165-3176, 2011.
3. K. Bliznakova, S. Suryanarayanan, A. Karellas, and N. Paiilikarakis, "Evaluation of an improved algorithm for producing realistic 3D breat software phantoms: Application for mammography," *Medical Physics*, vol. 37, pp. 5604-5617, 2010.
4. B. Chen, J. Shorey, R. S. J. Saunders, S. Richard, J. Thompson, L. W. Nolte, and E. Samei, "An anthropomorphic breast model for breast imaging simulation and optimization," *Academic Radiology*, vol. 18, pp. 536-546, 2011.
5. J. M. O'Connor, M. Das, C. Didier, M. Mah'D, and S. J. Glick, "Comparison of two methods to develop breast models for simulation of breast tomosynthesis and CT," in *Digital Mammography (IWDM)*, vol. 5116, *Lecture Notes in Computer Science*, E. A. Krupinski, Ed. Berlin-Heidelberg: Springer-Verlag, 2008, pp. 417-425.
6. F. Chen, D. D. Pokrajac, X. Shi, F. Liu, A. D. A. Maidment, and P. R. Bakic, "Partial Volume Simulation in Software Breast Phantoms," in *Physics of Medical Imaging*. San Diego, CA: SPIE, 2012.
7. G. B. Folland, *Advanced Calculus*. Upper Saddle River, NJ: Prentice-Hall, Inc., 2002.

Breast Image Registration
Using Non-Linear Local Affine Transformation

Feiyu Chen[a], Peng Zheng[a], Penglong Xu[a], Andrew D. A. Maidment[b],
Predrag R. Bakic[b], David D. Pokrajac[a], Fengshan Liu[a], Xiquan Shi[a]

[a]Delaware State University, 1200 N DuPont Hwy, Dover DE 19904;
[b]University of Pennsylvania, 3400 Spruce Street, Philadelphia, PA 19104

ABSTRACT

A novel breast image registration method is proposed to obtain a composite mammogram from several images with partial breast coverage, for the purpose of accurate breast density estimation. The breast percent density estimated as a fractional area occupied by fibroglandular tissue has been shown to be correlated with breast cancer risk. Some mammograms, however, do not cover the whole breast area, which makes the interpretation of breast density estimates ambiguous. One solution is to register and merge mammograms, yielding complete breast coverage. Due to elastic properties of breast tissue and differences in breast positioning and deformation during the acquisition of individual mammograms, the use of linear transformations does not seem appropriate for mammogram registration. Non-linear transformations are limited by the changes in the mammographic projections pixel intensity with different positions of the focal spot. We propose a novel method based upon non-linear local affine transformations. Initially, pairs of feature points are manually selected and used to compute the best fit affine transformation in their small neighborhood. Finally, Shepherd interpolation is employed to compute affine transformations for the rest of the image area. The pixel values in the composite image are assigned using bilinear interpolation. Preliminary results with clinical images show a good match of breast boundaries, providing an increased coverage of breast tissue. The proposed transformation can be controlled locally. Moreover, the method is converging to the ground truth deformation if the paired feature points are evenly distributed and its number is large enough.

Keywords: Digital mammography, image registration, affine transformation, Shepherd interpolation.

1. INTRODUCTION

Breast density, the relative amount of fat and dense tissue in the breast as seen in a mammogram, has been shown to be correlated with breast cancer risk. A number of methods[1][2] have been proposed to measure breast density from mammograms. However, some mammograms do not cover the entire patient's breast, e.g., due to large breast size in comparison to the x-ray imaging detector. This is of particular importance for the estimation of breast density, a biomarker of breast cancer risk. Partial breast visualization limits our ability to calculate breast density. One solution is to register and merge such partial mammograms, yielding complete breast coverage. Registration of mammograms is challenging because the mammogram is a 2D projection of non-rigid breast tissues. As a result, the 3D arrangement of the breast tissue is not exactly replicated in partial projections of large breasts. This is further complicated by differences in mammographic compression between images.

Registration techniques can be categorized as: 1) feature based techniques[3][4], which use feature points to match the images; 2) intensity based algorithms[5], which use the gray value of images; and 3) hybrid methods[6] that generate mapping between images (using feature points) with constraint on their intensity. For all of these registration techniques, a transformation must be determined so that the points in warped image can be related to their corresponding points in the reference image. Based on the number of degrees of freedom, the transformation models can use linear transformation (rigid and affine), elastic models or diffeomorphic transformations. Local controls cannot be achieved from the linear transformation model as the global parameters are computed for the entire image. The elastic model offer high order control, but the performance of elastic models is a balance between flexibility and computational complexity. Diffeomorphic transformations, which preserve topology, have resulted in good performance in a number of applications including brain MRI image registration.

The main difficulty of feature-based methods is to extract and match intrinsic feature points from mammograms, as there are no significant landmarks in a mammogram except the nipple. In this paper, a novel feature based approach, non-linear local affine transformation, is proposed to obtain a composite image from several images with partial breast coverage. Feature points are manually selected near the nipple, breast boundary and inside the

breast based upon visual similarity in both mammograms. Affine transformations between sets of feature points are then computed. Finally, Shepherd interpolation [7] is used to extend affine transformations to the entire breast. The pixel values in the composite image are assigned using the average of different images. Results with clinical images show that the resulting image cover different parts of original images, and the same texture from both registered images has a good agreement in composite image.

Qualitative testing is presented on selected images from the ACRIN DMIST database[8]. This work was tested with anonymized images obtained about IRB ethical review. A clinical image was split into two overlapping partial images; one partial image was transformed (the warped image), while another was not modified (the reference image). Those images were treated as a pair of mammograms with different coverage.

2. METHODOLOGY

2.1 Extraction of feature points

Our algorithm requires that feature points be extracted prior to registration, and the result of registration will depend on the reliability and accuracy of the extracted features. Automatic identification and extraction of feature points is difficult due to the non-linear compression deformation and the lack of significant landmarks in mammograms (Fig. 1). Typically, the features are the center of ROI, crossing points, end points and middle points. We observe the prominent features (such as ducts and blood vessels) from both images, Fig. 1. The crossing points are determined upon visual similarity in both mammograms. Due to compression and different positions of the breast, the coordinates of those crossing points may be different in the two mammograms, but the orientation of feature and local curvature of crossing points are more likely to be preserved. The advantage of our manual extraction is that the correspondence of two sets of feature points can be established during the extraction step. We also select other features (end points and middle points) in a small neighborhood around the selected crossing points. Subsequently, the deformation between two sets of feature points can be estimated.
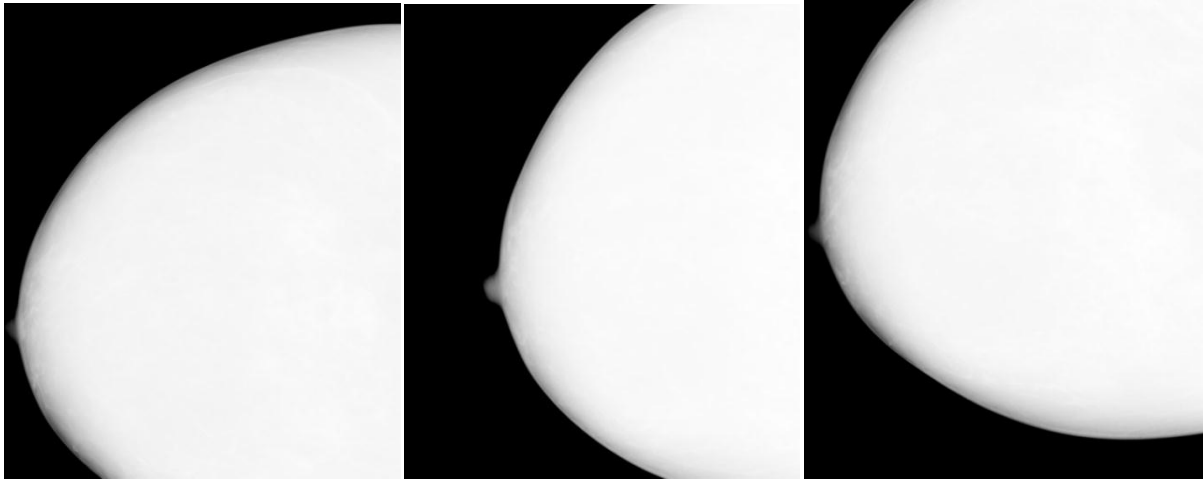
Figure 1: Three clinical images of the same patient from ACRIN DMIST database demonstrating partial breast coverage.

2.2 Best affine transformation

Given two sets of feature points in two images that need to be registered, we assume the deformation between them can be approximated by affine transformation, which can be considered as a first-order approximation of the true transformation resulting from breast projection.

We denote the two images obtained from different angle and different compression by I_1 and I_2, and assume $S_1 = \{X_1, X_2, \cdots, X_n\}$ be a set of feature points in I_1 (reference image), and $T_1 = \{Y_1, Y_2, \cdots, Y_n\}$ be the corresponding set in I_2 (warped image). Particularly, X_1 and Y_1 are the crossing points in each set, called the centers of S_1 and T_1. The affine transformation $\varphi : \varphi(x) = Ax + b$ mapping S_1 into T_1 can be obtained by solving the optimization problem:

$$\arg\min_{A\in R^2\times R^2, b\in R^2} \sum_{j=1}^{n}\left\|AX_j+b-Y_j\right\|^2 \qquad (1)$$

where A is a 2x2 matrix including scaling and rotation, $b \in R^2$ is a translation vector.

The solution of the above optimization problem can be expressed as:

$$[A,b]=\left([Y]_{2\times n}\begin{bmatrix}X\\1\end{bmatrix}^T_{n\times 3}\right)_{2\times 3}\left(\begin{bmatrix}X\\1\end{bmatrix}_{3\times n}\begin{bmatrix}X\\1\end{bmatrix}^T_{n\times 3}\right)^{-1}_{3\times 3} \qquad (2)$$

where $X=\lfloor X_1,X_2,\cdots,X_n\rfloor$ and $Y=\lfloor Y_1,Y_2,\cdots,Y_n\rfloor$.

Similarly, for each corresponding pairs of feature sets $(S_1,T_1),(S_2,T_2),\cdots,(S_k,T_k)$, we can also obtain the best affine transformations $\varphi_1,\varphi_2,\cdots,\varphi_k$ that minimize the least square error. Note that if we consider $\{\varphi_i\}$ as a basis, then for an arbitrary point in I_1, we can find its affine transformation by combining the basis with different non-linear weights [see equation (3) below].

2.3 Non-linear Local Affine Transformation

The Shepard interpolation [7], which is a simple case of inverse distance weighting to assign value to unknown points based on given points, is employed to compute the local affine transformation φ for each non-feature point in the image.
Assume X_i and Y_i are the centers of S_i and T_i, i.e., the affine transformation of X_i is φ_i, obtained from equation (2). For any other point Z in I_1, its corresponding local non-linear affine transformation φ is defined as:

$$\varphi(Z)=\begin{cases}\dfrac{\sum_{i=1}^{k}d_i^{-\alpha}\varphi_i}{\sum_{i=1}^{k}d_i^{-\alpha}} & \text{if } (\forall i\,)Z\neq X_i\\[2ex]\varphi_i & \text{if } (\exists i)Z=X_i\end{cases} \qquad (3)$$

where $d_i=|X_i-Z|$ is the Euclidean distance between X_i and Z. Note that non-linear deformation mapping φ is continuous since $\lim_{Z\to X_i}\varphi(Z)=\varphi_i$. Moreover, the partial derivatives with respect to two coordinates of φ exist at all the points if $\alpha>1$. We choose the default value of α as 2 for convenience of computation. The function $\varphi(Z)$ can be considered as the first order approximation of the ground truth deformation in a small neighbor of Z. It will converge to the ground truth deformation when the number of neighbors k is large enough and the feature points are evenly distributed. Note also that φ can be expressed locally as a linear combination of affine transformations. Moreover, local controls can be achieved if we add or delete feature sets in the region of interest.

The purpose of our image registration is mapping both I_1 and I_2 into same region to get composite image, say I_c. I_1 can be mapped to I_c by a translation transformation; while the non linear local affine transformation φ was used to estimate the mapping between I_2 and I_c, which will change the shape of image I_c.

In order to initialize the size of I_c, we have to determine the maximum and minimum value of I_2 under the local affine transformation $\varphi(x)$, where x can be represented by linear combination of four corner points c_j of I_2.

$$x=\sum_{j=1}^{4}w_j c_j \qquad \varphi(x)=\varphi(\sum_{j=1}^{4}w_j c_j)=\sum_{j=1}^{4}w_j\varphi(c_j). \qquad (4)$$

According to equation (3), we know that $\varphi(x)$, the local affine transformation at point x, is the linear average of φ_i with weight 1, therefore:

$$\max_{x}\varphi(x)=\max_{i}(\max_{j}\varphi_i(c_j)), \quad \min_{x}\varphi(x)=\min_{i}(\min_{j}\varphi_i(c_j)). \qquad (5)$$

Now we can classify I_c into four different regions R_1: the points x that have only inverse image y in I_1; R_2: the points x with inverse image z only from I_2; R_3: the points x that have inverse images y both in I_1 and in I_2; R_4:

the points that do not have any inverse image. The following strategy is used to assign gray values to the points in I_c.

$$I_c(x) = \begin{cases} I_1(y) & x \in R_1 \\ I_2(z) & x \in R_2 \\ \dfrac{I_1(y) + I_2(z)}{2} & x \in R_3 \\ 0 & x \in R_4 \end{cases} \qquad . \qquad (6)$$

2.4 Image validation method

The simplest validation is obtained from examination of the pixel-wise brightness difference between the reference image and the transformed warped image. However, such technique does not provide good performance for mammogram registration due to the 3D various projections of the breast tissues. Even if the positions of the image features are matched in the warped image and the reference image, the pixel brightness of same features will be different since the path of X-ray is different.

As an initial validation, individual clinical images were transformed to mimic partial coverage as illustrated in Fig. 2. A clinical image is split into two overlapping partial images. One partial image was transformed (the warped image) and another was not modified (the reference image). Those images were treated as a pair of mammograms with different coverage. The registration error can be computed as the difference between the original image and the composite image after the registration.
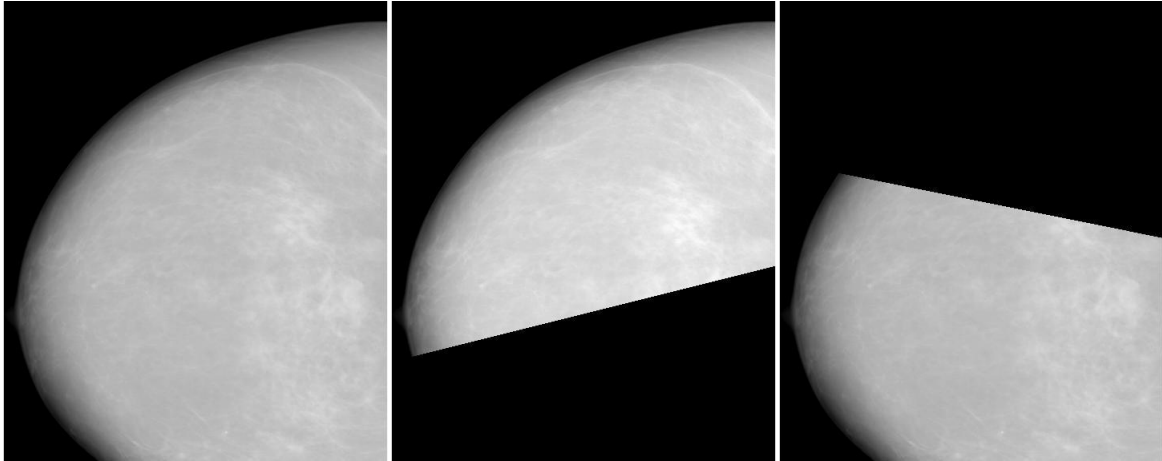

Figure 2: Original image and partial images (1 and 2) for validation.

3. RESULTS

In this section we present preliminary results using the proposed approach applied to clinic mammograms taken from the ACRIN DMIST database of mammograms. This work is a part of a larger study of racial disparity in breast cancer risk. For that project, breast percent density and parenchymal texture of minority women and age-matched Caucasian controls from the ACRIN DMIST database[8] are being compared.

Fig. 3 (a,b) illustrates the registration of two images from a large breast using the proposed non-linear local affine transformation with 9 pairs of feature sets. The effect of the choice of reference image is shown. Fig. 3c shows the composition of 3 partial views that covers the whole breast.

Fig. 4 illustrates the qualitative comparison of the proposed method with the result of Advanced Normalization Tools[9], (ANTs) that computes the unsupervised optimal diffeomorphic transformation by minimizing the similarity measure between warped image and reference image. The registered image of the warped image (Fig. 4a) and reference image (Fig. 4b) is shown in Fig. 4c. Fig. 4c illustrates the result of ANTs.
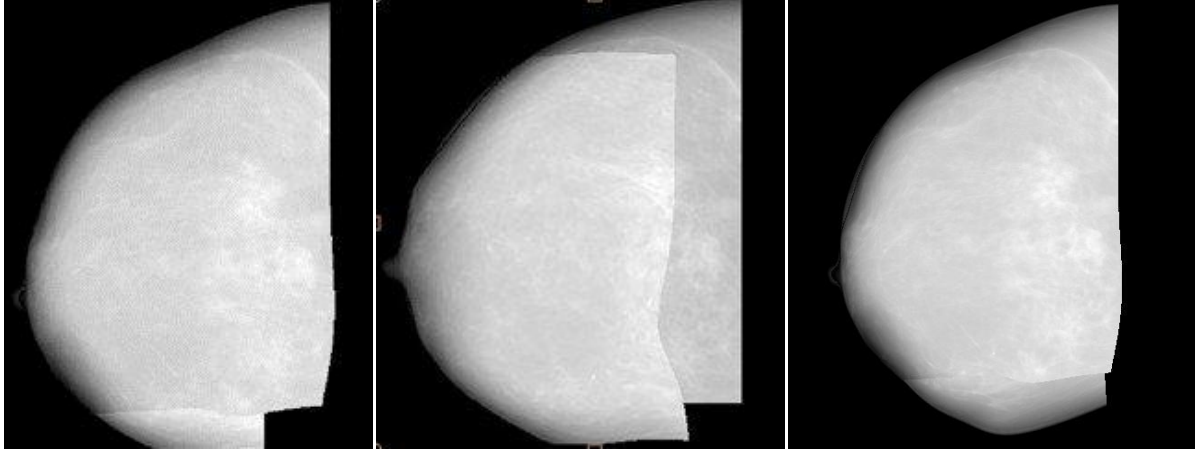
Figure 3a, b: Two partial images combined following registration, showing the effect of the choice of reference image. Figure 3c: The same breast showing the composition of three images in figure 1 after logarithm of grayscale values.

Fig. 5 illustrates the comparison of the original and the registered image. The reference (Fig. 5a) and the warped image (Fig. 5b) are obtained from Fig.2c. Fig. 5c illustrates the registered image using the proposed method, and Fig. 5d shows the difference between the composite and the original image (Fig. 1a after taking the logarithm).

4. DISCUSSION

To date, we have been able to achieve anecdotal results that support continued development and testing of this new method. Fig. 3 (a,b) suggests that the proposed method is robust, since the results of registration are similar regardless of the choice of the reference image (comparing Figs. 3a and 3b. Fig. 3 indicates that the observable features, especially the nipple and the boundary of skin, have good agreement.

Fig. 4 suggusts that the results of the proposed method are comparable to the results of the diffeomorphic transform implemented using ANTs, an open source software package. Particularly, the textures of warped image are preserved in registered images, and the shape of registered image is similar as reference image. The proposed method may have difficulties in registering some regions of the image (corresponding to region R_4, see equation (6)). Fig. 5 suggests that the features in the composite image show good agreement. The registration error is smaller in the region of overlap (the upper part of the registered image), since we can extract the corresponding feature points only from this region.

In our future work, we will apply the technique to more images in the DMIST database and develop statistical measures of the registration accuracy.

5. CONCLUSIONS

A novel registration task is proposed, and two methods are compared in this task. This study indicates that our newly proposed method may provide fast and comparatively accurate registration of overlapping breast images. The method may be of value whether used standalone or for initialization of other modern registration techniques (e.g., diffeomorphic transformation). The major drawback of the proposed method is the need for manual extraction of feature points. Further work is needed on application of automatic feature selection (e.g., SIFT algorithm [10]). Finally, we plan to perform more extensive quantitative validation of the proposed algorithm on a series reference and warped images extracted from all the applicable images in the ACRIN database.

6. ACKNOWLEDGMENT
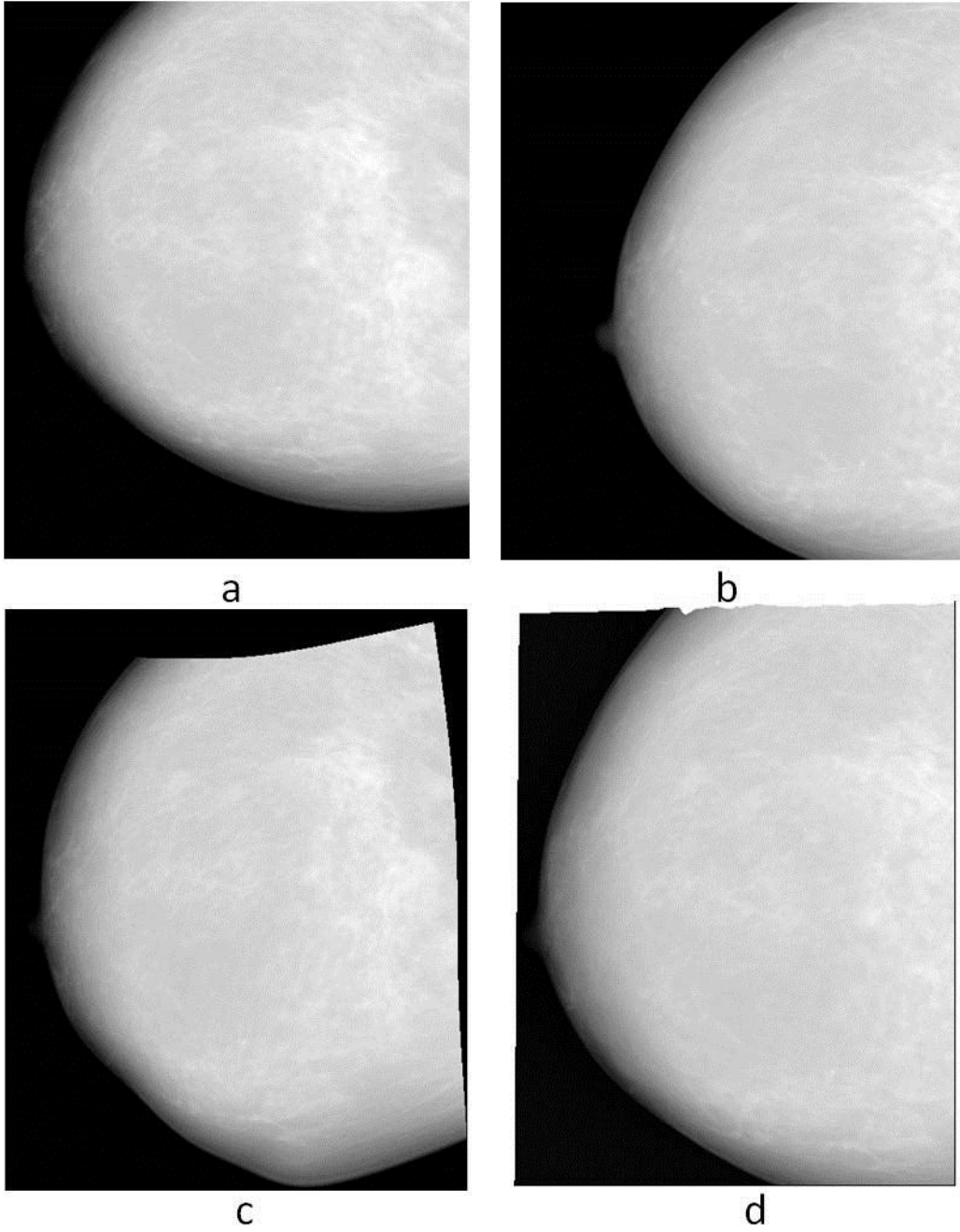
Figure 4: Warped image (a), reference image (b) and the result using the proposed method (c) and Advanced Normalization Tools (ANTs)[9] (d).
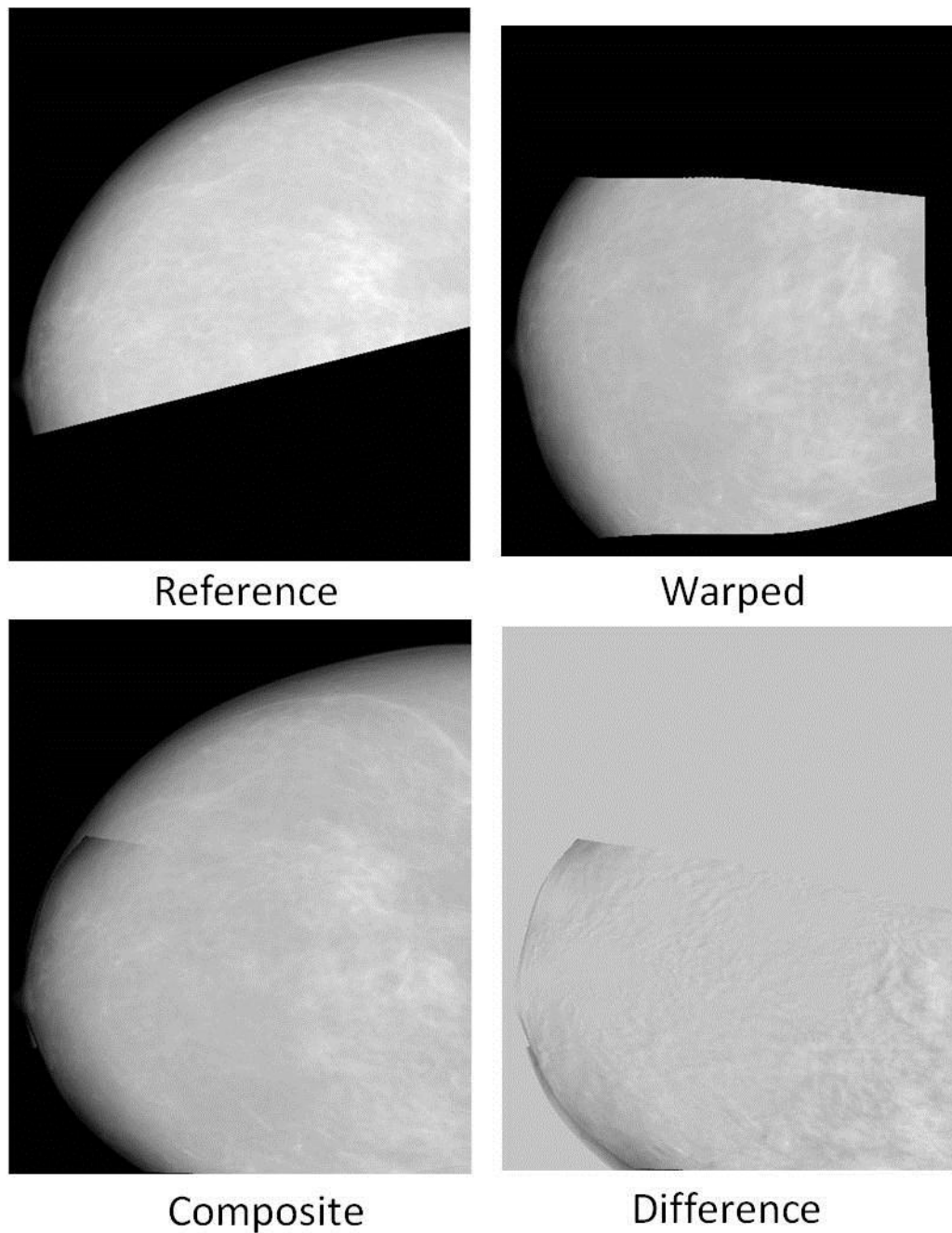
Figure 5: Example validation.

REFERENCES

1. McCormack VA, Highnam R, Perry N, dos Santos Silva I. Comparison of a new and existing method of mammographic density measurement: intramethod reliability and associations with known risk factors. *Cancer Epidemiol Biomarkers Prev. 16*, 1148–1154 (2007)
2. Kontos D, Bakic PR, Acciavatti RJ, Conant EF, Maidment ADA. A Comparative study of volumetric and area-based breast density estimation in digital mammography: result from a screening population. *Digital Mammography*. LNCS 6136:378–385.
3. Petroudi S, Brady M. Textons contours and regions for improved mammogram registration digital mammography. IWDM 2004, June 2004, Springer, Chapel Hill.

4.	Marti R, Zwiggelaar R, Rubin CME. Automatic mammographic registration: towards the detection of abnormalities. Detection of linear structures in mammographic images. *Medical image understanding analysis.* (2001)

5.	Brzakovic D, Vujovic N, Neskovicand M, Brzakovic P, Fogerty K (1996) Mammogram analysis by comparison with previous screenings. In: Doi K, Giger ML, Nishikawa RM,
Schmidt RA (eds) Digital Mammogrphy'96, Elsevier, Amsterdam

6.	Wirth MA, Narhan J, Gray D (2002) Nonrigid mammogram registration using mutual information. Proc SPIE 4684:562–573.

7.	Shepard, D. (1968) A two-dimensional interpolation function for irregularly-spaced data, Proc. 23rd National Conference ACM, ACM, 517-524.

8.	Pisano ED, Gatsonis C, Hendrick E, et al. Diagnostic Performance of Digital versus Film Mammography for Breast-Cancer Screening. NEJM 2005; 353:1773-1783.

9.	Avants BB, Tustison, N.J., Song, G., Gee, J.C., 2009. ANTS: Advanced Open-Source Normalization Tools for Neuroanatomy. Penn Image Computing and Science Laboratory.

10.	Lowe DG, Object recognition from local scale-invariant features. *Proceedings of the International Conference on Computer Vision*. 2. pp. 1150–1157.

Two Methods for Simulation of Dense Tissue Distribution in Software Breast Phantoms

Joseph H. Chui, Rongping Zeng*, David D. Pokrajac†, Subok Park*,
Kyle J. Myers*, Andrew D. A. Maidment, and Predrag R. Bakic

University of Pennsylvania, Department of Radiology, Philadelphia, PA
* Center for Devices and Radiological Health, Food and Drug Administration, Silver Spring, MD
† Computer and Information Sciences Department, Delaware State University, Dover, DE

{Joseph.Chui | Andrew.Maidment | Predrag.Bakic}@uphs.upenn.edu
DPokrajac@desu.edu {Rongping.Zeng | Subok.Park | Kyle.Myers}@fda.hhs.gov

ABSTRACT

Software breast phantoms have been developed for use in evaluation of novel breast imaging systems. Software phantoms are flexible allowing the simulation of wide variations in breast anatomy, and provide ground truth for the simulated tissue structures. Different levels of phantom realism are required depending on the intended application. Realistic simulation of dense (fibroglandular) tissue is of particular importance; the properties of dense tissue – breast percent density and the spatial distribution – have been related to the risk of breast cancer. In this work, we have compared two methods for simulation of dense tissue distribution in a software breast phantom previously developed at the University of Pennsylvania. The methods compared are: (1) the previously used Gaussian distribution centered at the phantom nipple point, and (2) the proposed combination of two Beta functions, one modeling the dense tissue distribution along the chest wall-to-nipple direction, and the other modeling the radial distribution in each coronal section of the phantom. Dense tissue distributions obtained using these methods have been compared with distributions reported in the literature estimated from the analysis of breast CT images. Qualitatively, the two methods produced rather similar dense tissue distributions. The simulation based upon the use of Beta functions provides more control over the simulated distributions through the selection of the various Beta function parameters. Both methods showed good agreement to the clinical data, suggesting both provide a high level of realism.

Keywords: Breast cancer imaging, anthropomorphic breast phantoms, software breast phantoms, validation, fibroglandular tissue distribution, Beta functions.

1. INTRODUCTION

Virtual Clinical Trials (VCTs) are emerging as a preclinical complement to clinical trials of breast imaging systems which are often longer and more expensive. In VCT, the simulations of breast anatomy, image acquisition, and model observers are combined to form a simulation pipeline. Realistic simulation of dense tissue is of particular importance since several properties of dense tissue may be used as imaging biomarkers of breast cancer risk. In this paper, we consider improvements to the glandular tissue distribution of the breast anatomy simulation component of the pipeline.

The 2D and volumetric fractional amount of dense tissue (called breast percent density) and the spatial distribution of dense tissue (called parenchymal texture) are known to correlate with cancer risk [1-7]. In this work we have compared two methods for simulation of dense tissue distribution in our software breast phantom design. The simulated distributions have been compared with distributions reported in the literature estimated from the analysis of breast CT images [8]. Covariance profiles estimated from phantom images, created with different methods for dense tissue simulation, are also compared to clinical data reported in the literature [11].

2. METHODS

Our proposed simulation of dense tissue is performed on breast phantoms created using a method proposed by Bakic et al [9]. In this proposed method, each simulated breast is divided into a predefined set of compartments. Each compartment consists of a seed point and a shape function. The seed point defines the compartment location, while the shape function defines its orientation. The values of seed points and shape functions are generated randomly based on a number of parameters defined by users. Each compartment is then labeled with different material types. Figure 1a) shows the cross section of a breast phantom where the compartments have not been labeled and figure 1b) shows a labeling of compartments to dense or fat tissues. A compartment is labeled as dense tissue if the criteria defined by the methods are met; or as fat tissue otherwise.

a)   b)
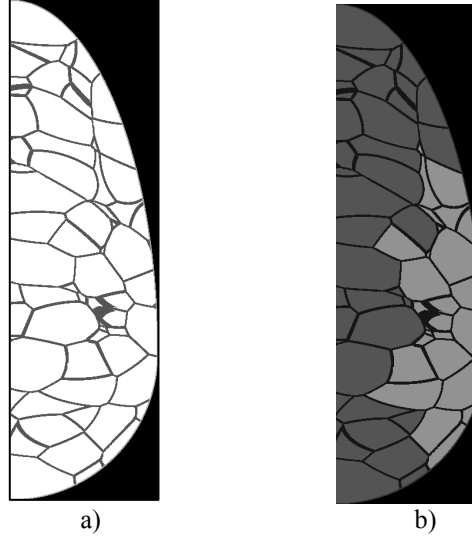
Figure 1. a) A cross section of simulated phantom. b) Each compartment inside the phantom is labeled with tissue types (light gray – dense, dark gray – fat).

A target number of compartments being labeled as dense is first determined based on a desired target volumetric breast density (VBD) defined by users. Each compartment is then assigned a probability of it being labeled as dense tissue, based on factors such as its location in the breast. Finally, each compartment is then labeled randomly based on its probability value.

2.1. Gaussian distribution method

The Gaussian distribution method for labeling dense components was originally proposed by Bakic et al [9]. In this method, the probability of a compartment labeled as dense tissue is determined by a Gaussian function:

$$p_G(\mathbf{s}_i) = \frac{\exp\left(-\sigma \cdot f_M^{\,2}(s_{xi} - a, s_{yi}, s_{zi})\right)}{Z} \tag{1}$$

where $f_M(.)$ represents the compartment shape function consistent with the quadratic decision boundaries described by a maximum *a posteriori* (MAP) classifier; a is the x coordinate of a simulated nipple point ($y = z = 0$), $\mathbf{s}_i$ (s_{xi}, s_{yi}, s_{zi}) are coordinates of seed vectors for the i-th compartment, and σ is a scaling coefficient. Z is a normalization constant chosen based upon a user-specified VBD of the phantom. In this method, the compartments near the nipple have a higher probability of being labeled as dense tissue compared to the ones further from the nipple.

2.2. Beta distribution method

In the Beta distribution method, the probability of a compartment labeled as dense tissue is determined by a function given by the product of two separate Beta functions:

$$p_B(\mathbf{s}_i) = \frac{Beta(\frac{s_{xi}}{a}; p_1, q_1) \times Beta(\frac{r_i}{R_i}; p_2, q_2)}{Z} \qquad (2)$$

where:

$$Beta(x; p, q) - \frac{1}{B(p,q)} x^{p-1}(1-x)^{q-1}, 0 \le x \le 1, B(p,q) = \int_0^1 t^{p-1}(1-t)^{q-1}dt,$$

s_{xi} is the distance of i-th seed point from the chest wall in posterior to anterior direction; r_i is the radial distance of seed point from center of its coronal slice; and R_i is the maximum radius of the coronal plane containing the i-th seed point.

Since these two beta functions are functions of distance in different directions, the distributions of dense tissue can be controlled separately in the chest wall to nipple direction and radial direction. Moreover, the shape of the beta function changes with different (p, q) values. Figure 2 shows two examples of beta function where the shapes are one-sided or two-sided depending on the values of (p, q).

a)   b)
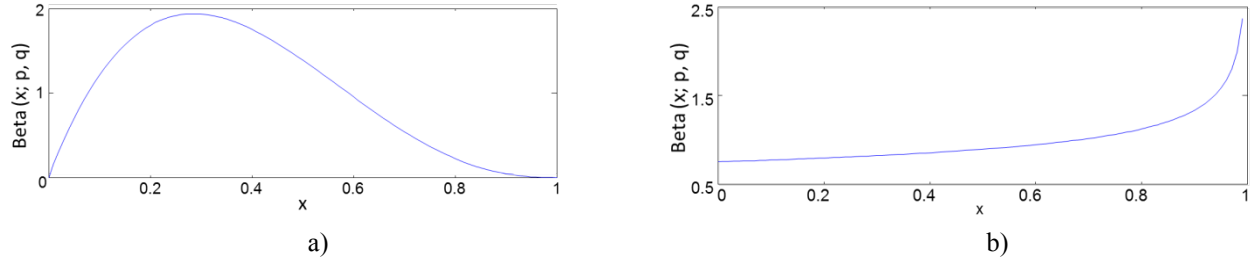
Figure 2: Beta distributions of two different (p, q) values: a) p = 2, q = 3.5; b) p = 1.0, q = 0.75.

2.3. Simulated acquisition of phantom images

Simulated mammograms are generated using software phantoms in a 2-step procedure. First, the breast deformation due to clinical mammographic compression is simulated by a finite element model [10]. The finite element model is implemented, using Abaqus (version 6.10-EF; Dessault Systèmes Americas, Waltham, MA), assuming a hyperelastic, almost incompressible material model for breast tissue, and 50% reduction in phantom thickness. Second, projection images of compressed phantoms are simulated using a ray-tracing method. The x-ray image acquisition model assumes a mono-energetic x-ray beam with the energy of 20 keV and an ideal detector with 100μm pixel size. The quantum noise is simulated by Poisson random variations and added to all simulated images.

2.4. Statistical analysis of phantom data

2.4.1. Analysis of dense tissue distributions

The dense tissue simulated using different methods are quantified using metrics defined in Huang et al [8], called Radial Glandular Fraction (RGF) and Coronal Glandular Fraction (CGF).

RGF and CGF are defined as

$$RGF_n(r) = \left\langle \left| \frac{N_D(r,x)}{N_D(r,x) + N_A(r,x)} \right| \right\rangle_{x \epsilon n} \qquad (3)$$

$$CGF(x) = \frac{N_D(x)}{N_D(x) + N_A(x)} \qquad (4)$$

where N_D is the number of pixels labeled as dense tissue, N_A is the number of pixels labeled as adipose tissue, and n indicates portion of breast, $n \in$ {Posterior, Middle Breast, Anterior}.

The RGF is used to quantify the distribution of simulated dense tissue based on the distance from center of the coronal slice in each region breast region (Posterior, Middle, and Anterior), while the CGF is used to quantify the distribution of simulated dense tissue in the posterior to anterior direction.

2.4.2. Analysis of covariance in simulated Images

Projection images were simulated for software phantoms with dense tissues labeled using either Gaussian or Beta distribution method with different sets of parameters. Covariance matrix elements [11] are defined as

$$K_{ij} = \langle (g_i - \overline{g_i})(g_j - \overline{g_j}) \rangle \, , \qquad (5)$$

where g_i and g_j are pixel values at the positions whose covariance is being estimated. The covariance matrix of each image set is assumed to be stationary; i.e. the covariance is independent of the location of their ROIs. We estimated covariance matrix elements along two orthogonal directions (chest-to-nipple and top-to-bottom) using ROIs of 4.35cm × 4.35cm in the regions of simulated images with constant thickness of the compressed phantom. A total number of 25 windows (1.45cm × 1.45cm) of 50% overlap in each ROI were used to calculate covariance matrix elements. To compare the covariance matrices of images simulated using different methods and parameters as well as with clinical data, the full width at half maximum (FWHM) of the average normalized covariance was used as the metric.

2.5. Materials

We compared the statistical properties of the phantom data to the clinical data reported in the literature [8] [11]. All phantoms were simulated with a breast volume of 450ml with resolution of 200μm per voxel. Each phantom contains 333 compartments randomly located and oriented inside the breast. Three phantom instances were simulated for each pair of distribution method/parameter and VBD value. The distribution parameters: σ in Gaussian method, and (p_1, q_1, p_2, q_2) in Beta method, were chosen manually based on user experience. Two sets of beta distribution parameters with different sidedness were chosen in order to interrogate the effects of the sidedness in beta functions. Table 1 shows the three sets of parameters used in the study.

**Table 1**. Distribution methods and parameter values used in the study.

Distribution methods	Parameter values
Gaussian	σ = 5.0
Beta1	p_1=2.0, q_1=0.5, p_2=2.0, q_2=3.5
Beta2	p_1=4.0, q_1=0.5, p_2=1.0, q_2=4.5

In our study, we created a total of 27 phantoms which consisted of 3 phantoms for each pair of VBD (20, 30, and 40%) and parameter in Table 1.

3. RESULTS

### 3.1. Probability maps of simulated dense tissue distribution

Probability values of dense tissue plotted on phantom surface provide a useful insight on the spatial characteristics of the method. Figure 3 shows the probability maps of phantoms created using the distribution parameters in Table 1. The probability map of Beta1 indicates a more uniformly distribution of probability, while Beta2 indicates a more concentrated probability near the nipple.
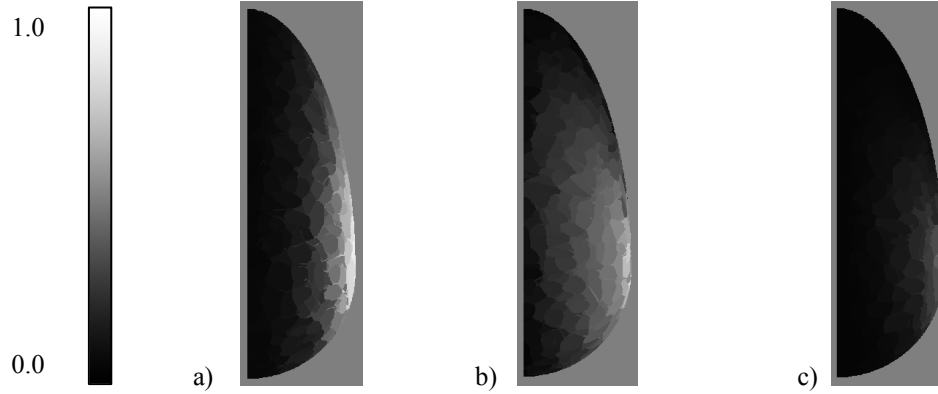
Figure 3: Probability maps of compartments labeled as dense tissues: a) Gaussian b) Beta1 and c) Beta 2.

3.2. Dense tissue simulation

Based on the probability values, calculated for each phantom compartment using the selected simulated method, the compartments are randomly labeled as containing dense or adipose tissue. Figure 4 shows the examples of phantoms of the same definition of compartment locations and orientations with dense tissue simulated using three sets of distribution parameters in Table 1. Compared to Gaussian and Beta2, dense tissue simulated using Beta1 are more distributed inside the breast.
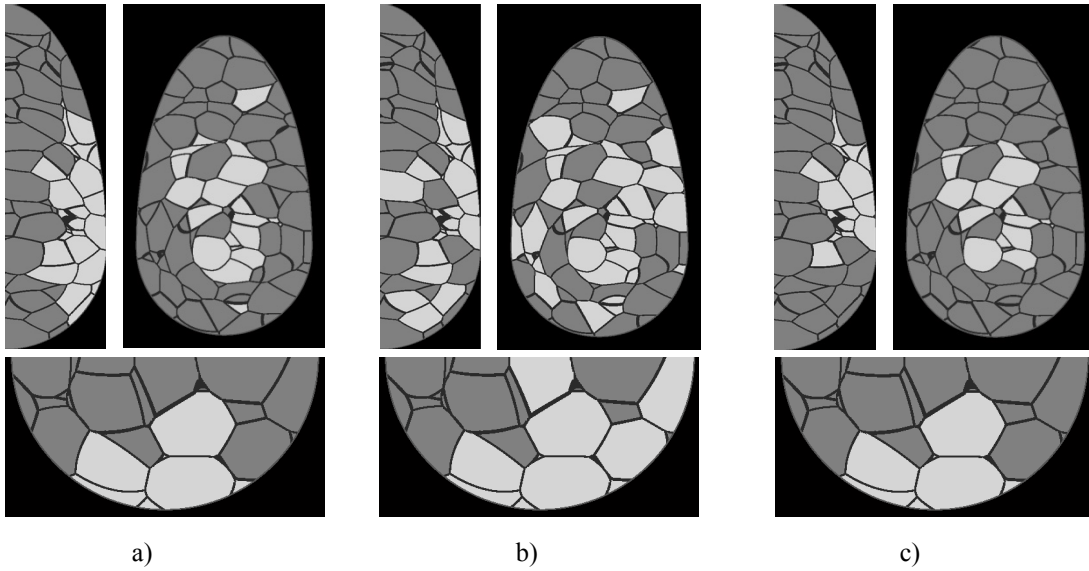
Figure 4: Phantoms with dense tissue simulated using a) Gaussian; b) Beta1; and c) Beta2.

3.3. RGF

The analysis of RGF is intended to compare dense tissue distributions simulated using different methods and parameters to clinical data, based on the radial distance from the center of the coronal plane. In order to have a close comparison with the clinical data, each breast phantom was divided into three equal thickness regions (Posterior, Middle, and Anterior). The RGFs were then measured separately in each of these three regions. Figure 5 a) to c) show the average RGFs of simulated phantoms using the three pre-defined parameters. Figure 5 d) to f) (the dash lines) show the average RGFs measured from the clinical data by Huang et al [8]. It was observed that the RGFs of the three distribution parameters in Table 1 result in similar trend as clinical data. Among the three distribution parameters, Beta2 method results in the best fit to the clinical data qualitatively.
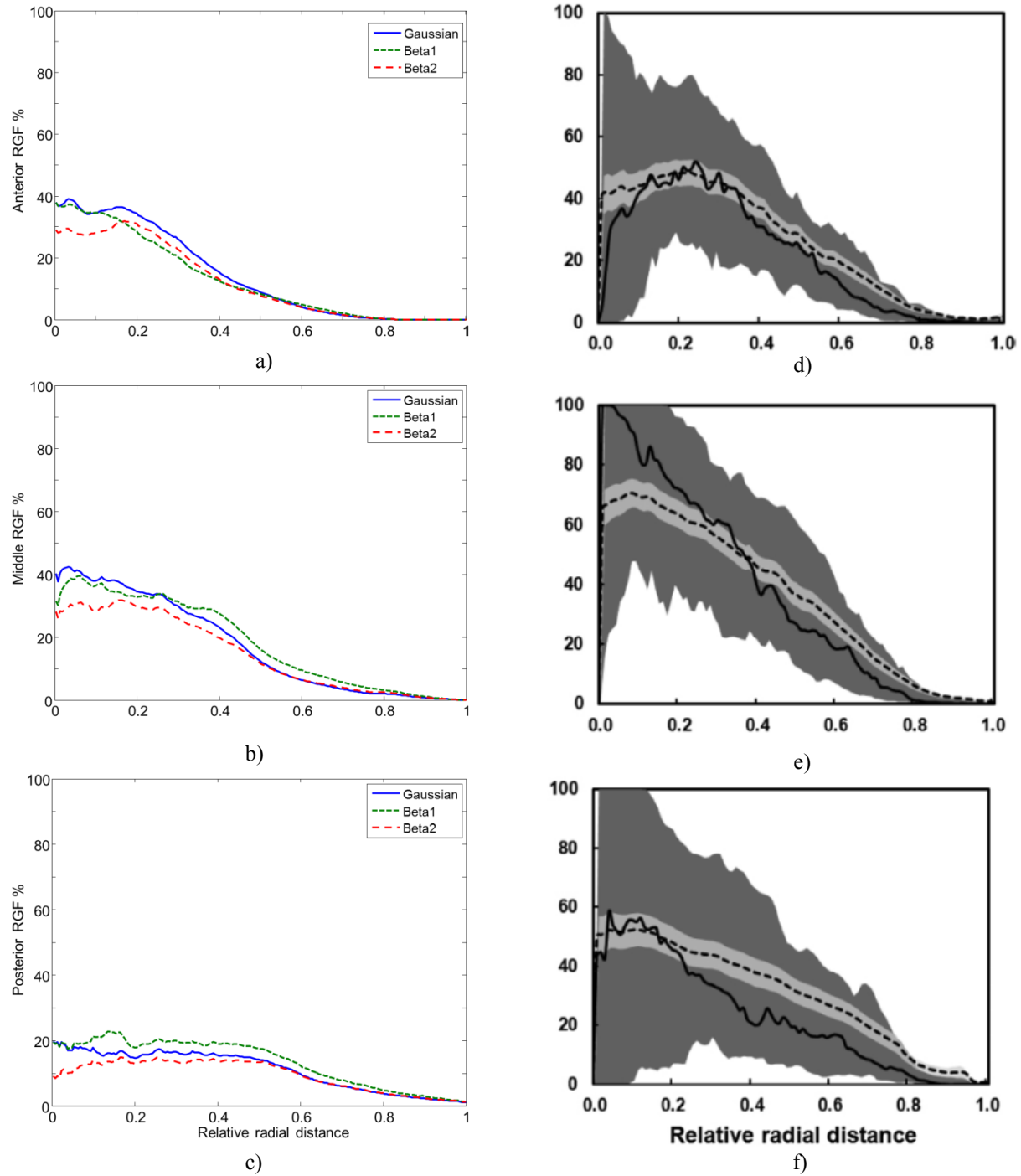
Figure 5: Average RGFs estimated from the simulated and clinical data. a)–c) The average RGFs in anterior, middle and posterior regions of simulated data, respectively. d)—f) The average RGFs in the respective regions, estimated from clinical data; (reprinted with permission from Huang et al. [8]). The total and 25-75 percentile regions are indicated by dark and bright colors, respectively. The mean and median values are indicated by dash and solid lines, respectively.

3.4. CGF

The analysis of CGF is intended to compare dense tissue distributions simulated using different methods and parameters to clinical data, based on the distance from the chest wall. Figure 6 a) shows the average CGFs measured from simulated distribution parameters in Table 1, and the dash line in Figure 6 b) shows the average CGFs measured from clinical data. Similar to the clinical data, the average CGFs measured from the simulated data increases with the coronal distance from the chest wall.
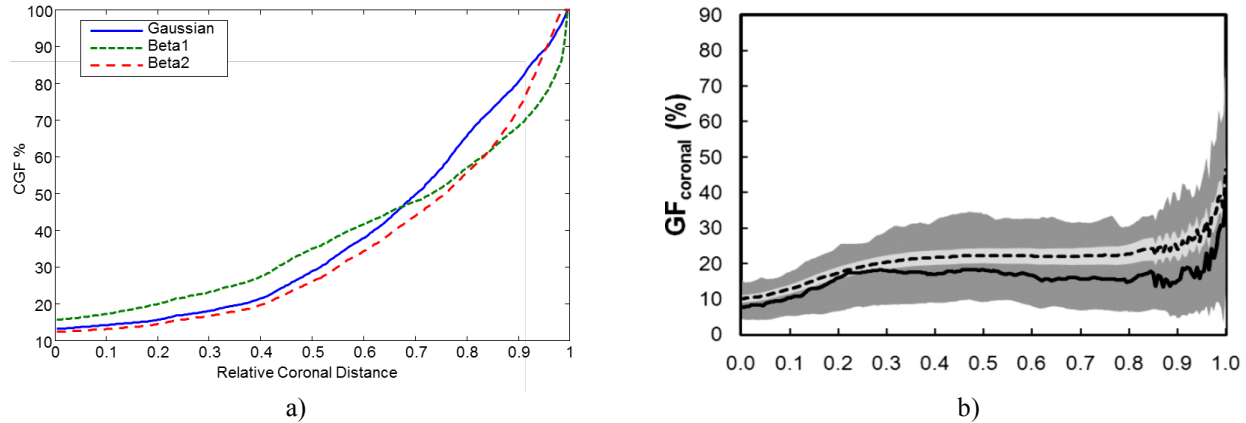
Figure 6: a) Average CGFs estimated from simulated data. b) Average CGFs (dash line) estimated from clinical data; (reprinted with permission from Huang et al [8].)

3.5. Simulated phantom images

Software phantoms created with different distribution methods and parameters are deformed to simulate breast compression during mammography acquisitions. Figure 7 shows the simulated acquisitions of phantoms with dense tissue created using the parameters in Table 1. Compared to Gaussian and Beta2, the dense tissue is more widely distributed in the image simulated using Beta1.
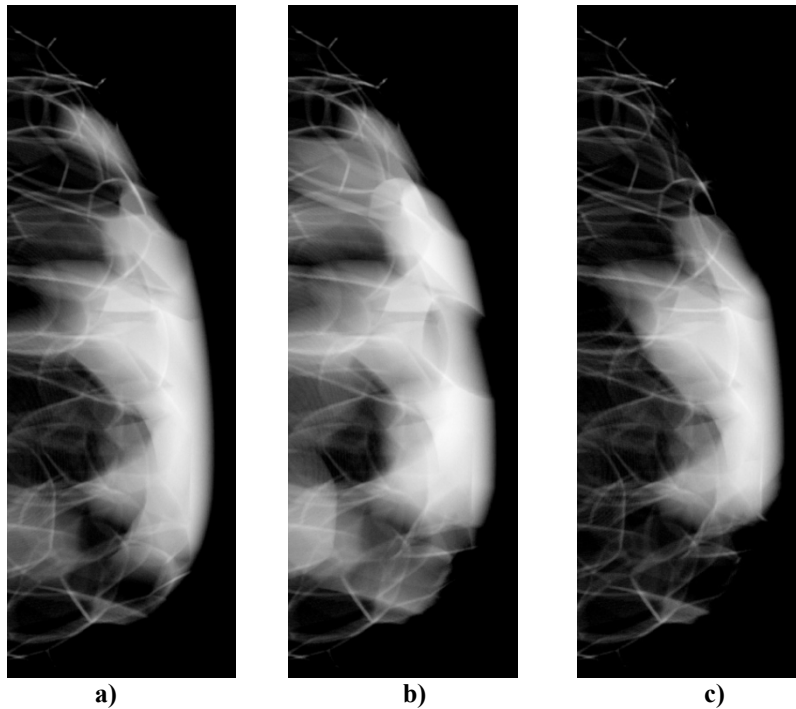
Figure 7: Simulated x-ray acquisition of phantoms using a) Gaussian method; b) Beta1 method; and c) Beta2 method.

3.6. Covariance analysis of simulated images

Average normalized covariance matrices measured from simulated acquisitions are shown in Figure 8 as function of the relative distance. The relative distance is equal to the spatial distance normalized by the window size used for estimating the covariance in the simulated images. Two windows are completely overlapped when the relative distance is 0, while only one row or column of pixels are overlapped when the relative distance is 1 or -1. The FWHMs of the average normalized covariance matrices are 0.381 (Gaussian), 0.433 (Beta1) and 0.344 (Beta2) for posterior-to-anterior direction; and 0.296 (Gaussian), 0.366 (Beta1) and 0.237 (Beta2) for top-to-bottom direction.
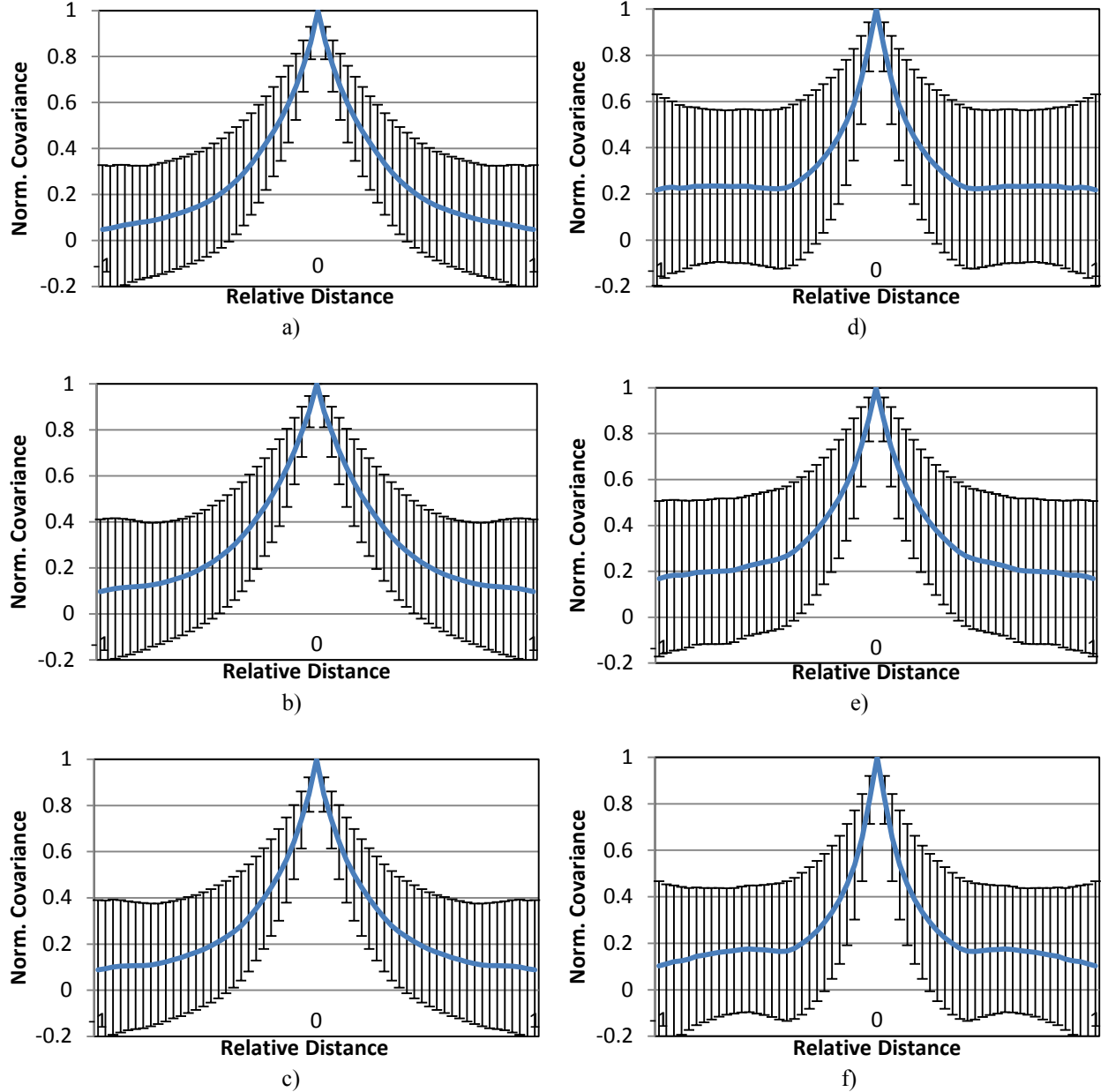
Figure 8: The profiles of average normalized covariance matrix measured from simulated acquisitions. Figure a) to c) are the profiles in posterior-to-anterior direction measured from a) Gaussian method; b) Beta1; and c) Beta2 method. Figures d) to f) are the respective profiles in top-to-bottom direction.

3.7. Comparing covariance profiles between simulated and clinical data

The covariance profiles in both posterior-to-anterior and top-to-bottom directions measured in simulated data are compared to ones measured from clinical data [11], using FWHM as the metric. Among the three distribution parameters in Table 1, Beta1 most closely matches the clinical data in both directions. Figure 9 shows the covariance profiles estimated from phantom images and clinical data. (Similar as in Figure 8, the relative distance is calculated as normalized by the window size used for the covariance calculation in the simulated images.)

a)   b)
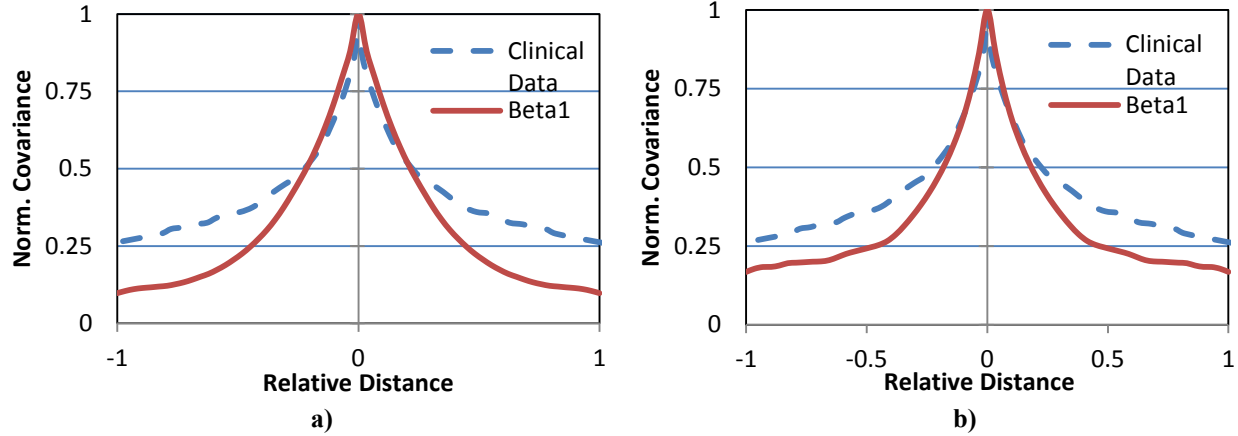
Figure 9: Profiles of average normalized covariance matrices in a) posterior-to-anterior direction; and b) top-to-bottom direction from simulated data created with Beta1 method and clinical data (modified from Freed et al. [11]). FWHMs measured from clinical data are 0.450(posterior-to-anterior) and 0.466 (top-to-bottom). FWHMs measured from simulated data using Beta1 are 0.433 (posterior-to-anterior) and 0.366 (top-to-bottom).

4. DISCUSSION

We implemented and compared the simulations of dense tissue using two different methods. Comparing to the Gaussian method using the Cartesian distance from the nipple, the Beta method separates the distance into radial and coronal distance. The use of beta functions offers higher control in the shape of distribution function such as its skewness and sidedness. The combination of extra flexibility in direction and the distribution functions provides additional freedom for the user to control the result of the dense tissue simulation.

The statistical properties such as RGF, CGF, and covariance matrices from data simulated using different methods and parameters shows Beta method has a better match to clinical data compared to Gaussian method. Careful optimization of the parameters in Gaussian method and in Beta method would be desirable to improve the matching between statistical properties measured in simulated and clinical data. Computing methods such as simulated annealing [12] and genetic programming [13] could be utilized for the tasks of parameter optimizations.

When comparing the RGFs of simulated versus clinical data near anterior breast region, a sudden drop off of glandular fraction is observed in the clinical data (Figure 5 a) and d)). The drop off is likely caused by the existence of subcutaneous fat around the nipple area. The existing simulation model used in our study does not correctly model the subcutaneous fat.

We observe a difference in normalized covariance between simulated and clinical data when the sampling windows are distant from each other. We believe that this could be the result of two factors. First it could be caused by the difference of ROI sizes used in simulated and clinical data. Smaller ROIs are used in measuring the simulated data, because of a restriction of the smaller region where uniform thickness exists in the compressed phantom. Second, there could be long distance correlations in the clinical data that are not modeled in the simulation.

5. CONCLUSION

We have proposed a novel method to assign dense compartments based upon Beta distributions. The new method offers better user control in spatial directions and shape of distribution function. We compared the simulated results with clinical images using CGF and RGF, and showed qualitative agreement. Future work includes quantitative evaluation of the agreement and selection of optimal distribution parameters.

ACKNOWLEDGEMENT

REFERENCES

[1] Wolfe, J.N.: Breast patterns as an index of risk for developing breast cancer. American Journal of Roentgenology 126, 1130-1139 (1976).

[2] Wolfe, J.N.: Risk for breast cancer development determined by mammographic parenchymal pattern. Cancer 37, 2486-2492 (1976).

[3] Boyd, N.F., Rommens, J.M., Vogt, K., Lee, V., Hopper, J.L., Yaffe, M.J. and Paterson, A.D.: Mammographic breast density as an intermediate phenotype for breast cancer. Lancet Oncol 6, 798-808 (2005).

[4] Li, H., Giger, M.L., Olopade, O.I., Margolis, A., Lan, L., Chinander, M.R.: Computerized texture analysis of mammographic parenchymal patterns of digitized mammograms. Academic Radiology 12, 863-873 (2005).

[5] Huo, Z., Giger, M.L., Olopade, O.I., Wolverton, D.E., Weber, B.L., Metz, C.E. and Zhong, W., Cummings, S.A.: Computerized analysis of digitized mammograms of brca1 and brca2 gene mutation carriers. Radiology 225, 519-526 (2002)

[6] Torres-Mejia, G., De, S.B., Allen, D.S., Perez-Gavilan, J.J., Ferreira, J.M., Fentiman, I.S. and Dos, S.S. I.: Mammographic features and subsequent risk of breast cancer: A comparison of qualitative and quantitative evaluations in the Guernsey prospective studies. Cancer Epidemiol Biomarkers Prev 14,1052-1059 (2005)

[7] Bakic, P.R., Carton, A.K., Kontos, D., Zhang, C., Troxel, A.B. and Maidment, A.D.: Breast percent density estimation from mammograms and central tomosynthesis projections. Radiology 2009-252(1):40-9.

[8] Huang, S.Y., Boone, J.M., Yang, K., Packard, N.J., McKenney, S.E., Prionas, N. D., Lindfors, K.K., Yaffe, M.J., The characterization of breast anatomical metrics using dedicated breast CT. Medical Physics 384, 2180-91 (2011).

[9] Pokrajac, D.D., Maidment, A.D.A., and Bakic, P.R. "Optimized generation of high resolution breast anthropomorphic software phantoms," Medical Physics, vol. 39, 2290-2302 (2012).

[10] Ruiter, N.V., Zhang, C., Bakic, P.R., Carton, A.-K., Kuo, J., Maidment, A.D.A.: "Simulation of tomosynthesis images based on an anthropomorphic breast tissue software phantom," In Visualization, Image-guided Procedures, and Modeling, Proc. SPIE 6918, edited by M.I. Miga, K.R. Cleary (2008).

[11] Freed, M., Badal, A., Jennings, R.J., De Las Heras, H., Myers, K. J., Badano, A., "X-ray properties of an anthropomorphic breast phantom for MRI and x-ray imaging," Phys Med Biol., vol. 56, 3513-33 (2011).

[12] Kirkpatrick, S., Gelatt, C. D., Vecchi, M. P., "Optimization by Simulated Annealing," Science, vol. 220, no. 4598, 671–680 (1983).

[13] Banzhaf, W., Nordin, P., Keller, R.E., and Francone, F.D., Genetic Programming: An Introduction: On the Automatic Evolution of Computer Programs and Its Applications, Morgan Kaufmann (1998).